J. Fluid Mech. (2006), *vol.* 569, *pp.* 151–184.
doi:10.1017/S0022112006002655 Printed in the United Kingdom

High-Reynolds-number steady flow in a collapsible channel

By J. C. GUNERATNE[1] AND T. J. PEDLEY[2]

[1]ARA, Manton Lane, Bedford, MK41 7PF, UK
julie.guneratne@ntlworld.com

[2]Department of Applied Mathematics and Theoretical Physics,
University of Cambridge, Wilberforce Road, Cambridge, CB3 0WA, UK

(Received 5 January 2005 and in revised form 12 April 2006)

We have studied steady flow in a two-dimensional channel in which a section of one wall has been replaced by an elastic membrane under dimensionless longitudinal tension T but possessing no bending stiffness. The dimensionless upstream transmural pressure takes a value P_{ext}, the membrane section is assumed to be long compared with the channel width and its deformation is assumed to remain within the viscous boundary layers. Standard high-Reynolds-number asymptotic methods are applied to arrive at a coupled boundary-layer-membrane problem. A non-zero cross-stream pressure gradient, leading to flow perturbations upstream of the membrane, is included in the analysis.

Linearization of the boundary-layer problem yields firstly an analytic solution at non-zero P_{ext} and asymptotically high T. This takes the form of an expansion in T^{-1} for which the membrane shape and the flow decouple at each order. Extension of this solution branch to smaller values of the tension suggests a singularity at finite tension, where the deformation of the membrane becomes very large. Secondly, when the upstream transmural pressure is zero the trivial solution is valid for all values of the tension. However, we also obtain eigensolutions where the membrane tension plays the role of eigenvalue. There are thus non-trivial solutions of the problem at these particular values of the tension.

The nonlinear coupled boundary-layer–membrane problem is then solved numerically. A finite-difference, Keller-box, marching scheme is used, together with a shooting algorithm to satisfy the boundary condition at the downstream end of the membrane. This reveals a variety of different solutions, showing the relation between the two cases captured by the linearized analysis and demonstrating the existence of parameter ranges for which no solutions exist under the specified constraints. Such parameter ranges appear not to exist if the downstream, rather than the upstream, transmural pressure is held constant.

The relation to our results of solutions obtained by solving the two-dimensional Navier–Stokes equations directly is discussed. Reasonable agreement between parameters is obtained, once allowance is made for the finite Reynolds number and membrane length in those computations.

1. Introduction

When fluid flows through a finite length of collapsible tube, mounted at its ends on rigid tubes and surrounded by a pressurized chamber, a wide range of behaviour is

observed. For example, even in steady conditions the relationship between the pressure drop along the collapsible segment, $\Delta\hat{p}$, and the flow rate $\hat{Q}$ may be concave to the $\hat{Q}$-axis ('pressure-drop limitation'), if the downstream transmural (external minus internal) pressure is held constant as $\hat{Q}$ is varied, but concave to the $\Delta\hat{p}$-axis ('flow-rate limitation') if the upstream transmural pressure is held constant. Moreover, in almost every experiment that has been performed on such a system, there are large areas of parameter space in which a rich variety of self-excited oscillations is observed, for values of the Reynolds number in excess of 100–200; see Conrad (1969) and Bertram, Raymond & Pedley (1991) for well-documented examples.

As yet a full computational simulation of this dynamical system, time-dependent and three-dimensional, has not proved feasible. In recent work by Hazel & Heil (2003), however, a thin-wall model for a collapsible tube, constrained to buckle into a two-lobed cross-section, is coupled to a steady three-dimensional Navier–Stokes solver.

Attempts to understand the mechanisms of the self-excited oscillations began with lumped-parameter (zero-dimensional) models governed by ordinary differential equations, in which very little of the mechanics could be rationally described (e.g. Katz, Chen & Moreno 1969), moved on to one-dimensional models in infinite tubes, which could not be coupled to the rest of the system (e.g. Shapiro 1977; Kamm & Shapiro 1979), and then to one-dimensional models in finite tubes, which could (e.g. Cancelli & Pedley 1985; Jensen & Pedley 1989; Jensen 1990). Self-excited oscillations were predicted and bore some resemblance to the observations, but still too much of the detailed mechanics was incorporated in an *ad hoc* manner that prevented confident quantitative comparison with experiment.

Luo & Pedley (1995, 1996) and Cai & Luo (2003) tried to provide a complete computational description of a two-dimensional version of the system that is in principle (though not yet in practice) realizable experimentally. This version (see figure 1) consists of a parallel-sided channel of which a segment of one wall is replaced by a membrane under constant tension, $\hat{T}$, but with no bending stiffness or inertia. The fluid flow is governed by the two-dimensional Navier–Stokes equations. The external pressure $\hat{p}_{ext}$ was fixed and positive relative to the pressure at the downstream end of the system, and the inflow rate was given in terms of the Reynolds number Re. (The different findings obtained when the upstream pressure is taken as reference are described in a later paper (Luo & Pedley 2000).) Steady flow was investigated first, and it was found (unexpectedly) that the variation in the maximum indentation, y_{max}, with $\hat{T}$ at given Re (or Re at given $\hat{T}$) agreed quite well with the corresponding one-dimensional model. Also, it was found that, as $\hat{T}$ was reduced for fixed $Re \geqslant 150$, self-excited oscillations arose when $\hat{T}$ fell below a critical value $\hat{T}_c$. At first these were relatively small-amplitude sinusoidal oscillations, suggesting a supercritical Hopf bifurcation but, as $\hat{T}$ was further reduced, additional bifurcations were seen, showing that the computational dynamical system, like the experimental one, had an intricate structure. However, the detailed mechanism by which the oscillations were generated and maintained remained unclear. Cancelli & Pedley (1985) had postulated that a crucial quantity was the energy dissipation associated with the separated jet from the narrowest point, but they modelled it quasi-steadily. Luo & Pedley (1996) therefore computed the energy dissipation per unit volume in the flow, but found in most cases that it was a maximum in the viscous boundary layers upstream of the narrowest point. Pedley & Luo (1998) suggested that there might be a coupling between the membrane oscillation and the vorticity waves generated in the channel downstream, and this would involve the process of flow separation, which computed streamline plots showed to be far from quasi-steady.

To shed further light it is desirable to have a mathematical model of the two-dimensional system which avoids the *ad hoc* assumptions of the one-dimensional models and which can be solved analytically and interrogated in detail in some asymptotic limit. Pedley (1992) published a model based on lubrication theory; this model is a rational approximation but is inertia free and cannot yield oscillations. The only other hope seems to be an asymptotic theory for high Reynolds number and small membrane displacement. This we embark upon here. Of course, we do not expect an asymptotic analysis to provide a full description of every mode of disturbance that could arise in a collapsible channel at infinitely large Reynolds number. In reality, the flow would become turbulent via a variety of fluid-dynamic instabilities, some of which would be modified by the presence of a compliant boundary but most of which would exist even if the boundary were fixed (see Gajjar & Türkyilmazoğlu 2000, for example). Instead, we seek a flow that can be thought of as the high-Reynolds-number extension of the branch of solutions to the full problem containing the steady flows and particular self-excited oscillations computed by Luo & Pedley (1995, 1996).

Even with the constraints of high Reynolds number and small membrane displacement, the problem is complex and various approaches are possible. Jensen & Heil (2003) took the limit of large membrane tension for which, in the absence of a mean throughflow and of viscosity, the system exhibits a set of normal-mode oscillations of high frequency. The lowest of these takes the form of a 'sloshing' mode in which in-and-out vibrations of the membrane are accompanied by longitudinal flows in the up- and downstream rigid-channel segments. The introduction of viscosity provides damping, in Stokes layers on the channel walls, and the introduction of a moderate (but still high-Reynolds-number) throughflow provides a source of energy that can be converted into growth of the oscillations by Reynolds stresses in the Stokes layers. Jensen & Heil were able to calculate, both asymptotically and computationally, a critical Reynolds number for instability at a given membrane tension (or vice versa), but they found that there would be no instability if the upstream rigid segment were longer than the downstream one or if the upstream inflow rate were fixed instead of the upstream pressure. The oscillations computed by Luo & Pedley (1996) arose even when the inflow rate was fixed, however, implying a different instability mechanism.

Here we embark on a different asymptotic approach and restrict our attention to steady flows. The approach is based firmly on the work of Smith (1976*a*, *b*), who pioneered the analysis of high-Reynolds-number internal flows in indented channels. Previous attempts to couple such internal boundary-layer flows with compliant walls were made by Tutty (1984) and by Rothmayer (1989). Recent review articles, e.g. Heil & Jensen (2003) and Grotberg & Jensen (2004), give further discussion of flow and oscillations in collapsible tubes.

An outline of the present paper is as follows. The steady-flow structure is described and the coupled boundary-layer–membrane problem is formulated in § 2. The problem can be solved (essentially) analytically for very small membrane displacement (which requires either large tension or small transmural pressure difference), and the solution is provided in § 3. Findings include the multiple non-uniqueness of the flow for very small tension and transmural pressure difference. Then in § 4 the nonlinear boundary-layer problem is solved numerically, confirming the finding of multiple non-uniqueness for given tension and upstream transmural pressure difference. The structure of the solution space is discussed and the effect of fixing the transmural pressure at the downstream, rather than the upstream, end is also considered.

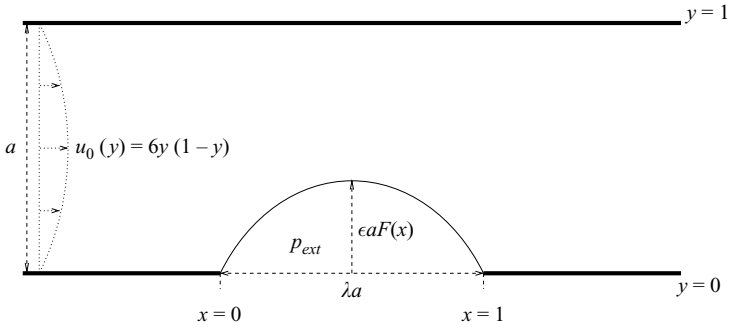

FIGURE 1. Diagram of the two-dimensional channel, width a, all other quantities being dimensionless, showing an incoming Poiseuille flow. The function $F(x)$ is used to represent the deformation of the section of membrane and the position of the solid wall that forms the rest of the lower boundary.

2. Formulation

2.1. *Non-dimensionalization and scaling*

The geometry under consideration is shown in figure 1, and is that of a channel of width a with a small-amplitude flexible deformation, of finite length λa where $\lambda \gg 1$, in one wall. We then use a Cartesian coordinate system $(\hat{x}, \hat{y})$, where $\hat{x}$ is aligned with the channel and $\hat{y}$ forms the transverse coordinate, with velocity components $\hat{u}, \hat{v}$ respectively and pressure $\hat{p}$. The problem is non-dimensionalized as follows:

$$(\hat{x}, \hat{y}) = (\lambda a x, a y), (\hat{u}, \hat{v}) = \bar{U}(u, v/\lambda), \hat{p} = \rho \bar{U}^2 p, \tag{2.1}$$

where $\bar{U}$ is the mean velocity far upstream and ρ is the density of the fluid.

Since only steady configurations of the channel are considered, the position of the lower boundary of the flow domain is given by

$$y = \epsilon F(x),$$

where $\epsilon \ll 1$; the function F is constrained to be zero when $x < 0$ or $x > 1$, where it represents solid wall, and is everywhere continuous. The flow is then governed by the steady dimensionless Navier–Stokes equations, with the long streamwise length scale λa given above:

$$u_x + v_y = 0, \tag{2.2a}$$

$$\lambda^{-1}(u u_x + v u_y) = -\lambda^{-1} p_x + Re^{-1}(\lambda^{-2} u_{xx} + u_{yy}), \tag{2.2b}$$

$$\lambda^{-1}(u v_x + v v_y) = -\lambda p_y + Re^{-1}(\lambda^{-2} v_{xx} + v_{yy}), \tag{2.2c}$$

where $Re = \bar{U}a/\nu$ is the Reynolds number and ν is the kinematic viscosity of the fluid.

The boundary conditions are those of zero penetration and no slip,

$$u = v = 0 \quad \text{on} \quad y = 1, \tag{2.3a}$$

$$u = v = 0 \quad \text{on} \quad y = \epsilon F, \tag{2.3b}$$

at the walls. The velocity profile is taken to be parabolic far upstream,

$$u \to u_0(y) = 6y(1 - y) \quad \text{as} \quad x \to -\infty, \tag{2.3c}$$

$$v \to 0 \quad \text{as} \quad x \to -\infty, \tag{2.3d}$$

where the factor 6 is chosen to make the average velocity 1. The flow is assumed to remain a small perturbation to Poiseuille flow, of $O(\epsilon)$, throughout the domain.

The membrane is assumed to be under tension and to have no bending stiffness, so the pressure field is coupled with the position of the lower boundary via

$$\left.\begin{aligned} p(x,0) - p_{ext} = \bar{T}\,\epsilon\, F_{xx} \quad & 0 \leqslant x \leqslant 1, \\ F \equiv 0 \quad & \text{otherwise,} \end{aligned}\right\} \tag{2.4}$$

where p_{ext} is the dimensionless pressure external to the channel and $\bar{T}$, the dimensionless tension, is assumed constant over the membrane to the order at which we are working. $\bar{T}$ is related to the dimensional tension $\hat{T}$ via

$$\hat{T} = \bar{T}\rho\bar{U}^2\lambda^2 a. \tag{2.5}$$

The dimensionless dissipation per unit volume, using the scalings (2.1), is

$$\phi = \frac{1}{Re}\left(\left(u_y + \frac{v_x}{\lambda^2}\right)^2 - \frac{4u_x v_y}{\lambda^2}\right). \tag{2.6}$$

2.2. *Core flow*

Following Smith (1976*a*), with the notation of Pedley (2000), we express the inviscid flow in the core of the channel as an asymptotic expansion in powers of ϵ and see that the effect of the wall deformation upon the inviscid core flow is simply a streamline displacement of magnitude $-\epsilon A(x)$:

$$u = u_0(y) + \epsilon A(x)u_0'(y) + O(\epsilon^2), \tag{2.7a}$$

$$v = -\epsilon A_x(x)u_0(y) + O(\epsilon^2), \tag{2.7b}$$

$$p = -\frac{12\lambda x}{Re} + \epsilon^2\left(\tilde{P}(x) + \frac{A_{xx}}{\lambda^2\epsilon}\int_0^y u_0^2(y')\,\mathrm{d}y'\right) + O(\epsilon^3), \tag{2.7c}$$

where $A(x)$ and $\tilde{P}(x)$ are unknown functions and $12\lambda x/Re$ represents the Poiseuille pressure gradient. The second term within the large parentheses represents the cross-stream pressure gradient and is negligible if $\lambda^2\epsilon \gg 1$; we assume that $\lambda^2\epsilon$ is $O(1)$ or larger.

Substituting the expansions (2.7) into (2.6), we obtain the dissipation in the core,

$$\phi = \frac{1}{Re}\left(u_0'^2 + 2\epsilon u_0'u_0''A + O\left(\epsilon^2, \frac{\epsilon}{\lambda^2}\right)\right).$$

Integrating this over the region $x \in (x_0, x_1)$, $y \in (\epsilon F, 1)$, we obtain the total dissipation arising from the core flow,

$$\frac{12}{Re}(x_1 - x_0) - \frac{12\epsilon}{Re}\left(3\int_0^1 F(x)\,\mathrm{d}x + 2\int_{x=x_0}^{x_1} A(x)\,\mathrm{d}x\right) + O\left(\frac{\epsilon^2}{Re}, \frac{\epsilon}{\lambda^2 Re}\right),$$

where the leading-order term is simply the dissipation arising from the unperturbed Poiseuille flow.

2.3. *Boundary layers*

The velocity perturbation in (2.7*a*) does not satisfy the no-slip condition on the channel walls so there must be a viscous boundary layer on each. For the viscous and inertial terms to balance, the thickness of the boundary layer must be $O((\lambda/Re)^{1/3})$. We assume that the wall deformation remains within the viscous boundary layer in order that the expansions (2.7) may be uniformly asymptotic over the entire core

region and hence that

$$\epsilon = \left(\frac{\lambda}{Re}\right)^{1/3}, \tag{2.8}$$

which also ensures that the pressure gradient appears at the same order as the advective terms in the boundary-layer equations, (2.11), (2.13) below. The Poiseuille pressure gradient is then an $O(\epsilon^3)$ term, so the rescalings for the upper (rigid-wall) and lower (deformed-wall) boundary layers, where the latter includes a Prandtl transformation, are given by

$$1 - y = \epsilon z, \quad u = \epsilon U, \quad v = -\epsilon^2 V, \quad p = \epsilon^2 P(x), \tag{2.9}$$

$$y - \epsilon F = \epsilon \tilde{z}, \quad u = \epsilon \tilde{U}, \quad v = \epsilon^2 \tilde{V} + \epsilon u F_x, \quad p = \epsilon^2 \tilde{P}(x). \tag{2.10}$$

We thus obtain a pair of coupled boundary-layer problems: on the plane wall

$$U_x + V_z = 0, \tag{2.11a}$$

$$UU_x + VU_z = -P_x + U_{zz}, \tag{2.11b}$$

$$U = V = 0 \quad \text{at} \quad z = 0, \tag{2.12a}$$

$$U \to 6z,\ V \to 0 \quad \text{as} \quad x \to -\infty, \tag{2.12b}$$

$$U \sim 6(z - A) \quad \text{as} \quad z \to \infty; \tag{2.12c}$$

and on the deformed wall

$$\tilde{U}_x + \tilde{V}_{\tilde{z}} = 0, \tag{2.13a}$$

$$\tilde{U}\tilde{U}_x + \tilde{V}\tilde{U}_{\tilde{z}} = -\tilde{P}_x + \tilde{U}_{\tilde{z}\tilde{z}}, \tag{2.13b}$$

$$\tilde{U} = \tilde{V} = 0 \quad \text{at} \quad \tilde{z} = 0, \tag{2.14a}$$

$$\tilde{U} \to 6\tilde{z},\ \tilde{V} \to 0 \quad \text{as} \quad x \to -\infty, \tag{2.14b}$$

$$\tilde{U} \sim 6(\tilde{z} + F + A) \quad \text{as} \quad \tilde{z} \to \infty, \tag{2.14c}$$

where the boundary conditions in each case specify no-slip and no penetration on the wall or membrane, the upstream condition and the condition of matching to the core flow, respectively.

The relation between the pressure in the two boundary layers is seen from (2.7c) to be

$$P = \tilde{P} + \sigma A_{xx}, \tag{2.15}$$

where $\sigma = 6/5\lambda^2\epsilon$ is the cross-stream pressure-gradient parameter. Note that the scaling specified for ϵ above, (2.8), implies that

$$\sigma = \frac{6Re^{1/3}}{5\lambda^{7/3}},$$

and hence the requirement that σ and ϵ both be small implies that $Re^{1/7} \ll \lambda \ll Re$. A non-zero cross-stream pressure gradient implies that $\sigma = O(1)$, i.e. $\lambda = O(Re^{1/7})$.

If the cross-stream pressure gradient is negligible, i.e. $\sigma \ll 1$, then the pressures in the two boundary layers are the same. Equations (2.11a, b), and (2.12a, b) for U and V are then identical to (2.13a, b), and (2.14a, b) for $\tilde{U}$ and $\tilde{V}$, so if the boundary-layer equations have a unique solution for a given wall deformation (and hence, in this case, a given pressure field) the two matching conditions must also be identical. Equating the

matching conditions (2.12*c*) and (2.14*c*) we then see that, as found by Smith (1976*a*),

$$A(x) = -F(x)/2, \tag{2.16}$$

and the problem has been reduced to that of the flow in a single boundary layer coupled to the deformation of the membrane.

The dissipation in the upper boundary layer is, from (2.6) and (2.9),

$$\phi = \frac{1}{Re}\left(U_z^2 + O\left(\frac{\epsilon^2}{\lambda^2}\right)\right)$$

and similarly in the lower boundary layer. If U_z is $O(1)$ over an $O(1)$ area in (x, z)-space, then the dissipation in the boundary layer is $O(1/Re)$, which is of the same order as the Poiseuille dissipation.

Finally, we rewrite the membrane equation in the form

$$\left.\begin{aligned} \tilde{P} - P_{ext} &= T F_{xx} \quad 0 \leqslant x \leqslant 1, \\ F &\equiv 0 \qquad \text{otherwise,} \end{aligned}\right\} \tag{2.17}$$

where $p_{ext} = \epsilon^2 P_{ext}$ and $\bar{T} = \epsilon T$. Note that this implies $|p_{ext}|/\bar{T} = O(\epsilon) = O((\lambda/Re)^{1/3})$.

A choice must be made of where to fix the fluid pressure, upstream or downstream. This makes a difference experimentally, as described in the introduction, and we shall investigate that difference here. For now we take the upstream fluid pressure to be fixed: $\tilde{P}(-\infty) = 0$.

2.3.1. *Linearization of the boundary-layer equations*

In § 3 we will solve a linearized form of the boundary-layer equations: if the deformation F is small, this implies that the perturbations to the internal pressure and velocity scales are similarly small. Introducing a small parameter h, we write

$$\begin{aligned} &F(x) = hF(x), \quad P(x) = hP(x), \quad U(x,z) = 6z + hU(x,z), \quad V(x,z) = hV(x,z), \\ &A(x) = hA(x), \quad \tilde{P}(x) = h\tilde{P}(x), \quad \tilde{U}(x,\tilde{z}) = 6\tilde{z} + h\tilde{U}(x,\tilde{z}), \quad \tilde{V}(x,\tilde{z}) = h\tilde{V}(x,\tilde{z}). \end{aligned} \tag{2.18}$$

With a further transformation to express the equations in terms of the shear-rate perturbations,

$$\tau = U_z, \quad \tilde{\tau} = \tilde{U}_{\tilde{z}},$$

the linearized boundary-layer equations may be cast into the following form:

$$6z\tau_x = \tau_{zz}, \tag{2.19a}$$

$$\tau_z = P_x \quad \text{at} \quad z = 0, \tag{2.19b}$$

$$\tau \to 0 \quad \text{as} \quad z \to \infty, \tag{2.19c}$$

$$\tau \to 0 \quad \text{as} \quad x \to -\infty, \tag{2.19d}$$

$$\int_0^\infty \tau \, \mathrm{d}z = -6A \tag{2.19e}$$

and

$$6\tilde{z}\tilde{\tau}_x = \tilde{\tau}_{\tilde{z}\tilde{z}}, \tag{2.20a}$$

$$\tilde{\tau}_{\tilde{z}} = \tilde{P}_x \quad \text{at} \quad \tilde{z} = 0, \tag{2.20b}$$

$$\tilde{\tau} \to 0 \quad \text{as} \quad \tilde{z} \to \infty, \tag{2.20c}$$

$$\tilde{\tau} \to 0 \quad \text{as} \quad x \to -\infty, \tag{2.20d}$$

$$\int_0^\infty \tilde{\tau} \, \mathrm{d}\tilde{z} = 6(F + A). \tag{2.20e}$$

Equations (2.19*b*) and (2.20*b*) were derived by evaluating the streamwise momentum equations, (2.11*b*), (2.13*b*), on $z = 0$ and $\tilde{z} = 0$ respectively.

Applying the rescalings (2.18) to the pressure relation (2.15), we obtain the relation between the pressures in the two boundary layers,

$$P = \tilde{P} + \sigma A_{xx}. \tag{2.21}$$

The membrane equation (2.17) becomes

$$\begin{aligned} hP - P_{ext} &= hTF_{xx} \quad 0 \leqslant x \leqslant 1, \\ F &\equiv 0 \qquad\quad \text{otherwise.} \end{aligned} \tag{2.22}$$

For consistency this requires $|P_{ext}/T| = O(h)$, or $\left|p_{ext}/\bar{T}\right| = O(h(\lambda/Re)^{1/3})$.

3. Solution of the linearized problem

We discuss first the solution of the linearized boundary-layer equations for the flow past a given wall deformation $F(x)$, as obtained by Smith (1976*a*), before analysing the coupling of the flow to the membrane position both in the case when the external pressure is zero (i.e. equal to the internal pressure at the upstream end of the flow domain) and when it is non-zero.

3.1. *Linearized boundary-layer flow past a prescribed deformation*

The linearized boundary-layer equations may be solved for A, P, $\tilde{P}$, $\tau(x, 0)$ and $\tilde{\tau}(x, 0)$ in terms of the membrane displacement F using Fourier-transform methods as described by Smith (1976*b*). Under the Fourier transform

$$\phi^*(k, z) = \int_{-\infty}^{\infty} \phi(x, z) \mathrm{e}^{-\mathrm{i}kx}\, \mathrm{d}x,$$

(2.19*a*) reduces to the Airy equation in $\zeta = (6\mathrm{i}k)^{1/3}z$, and we may thus write

$$\tau^*(k, z) = B^*(k)\mathrm{Ai}(\zeta), \tag{3.1}$$

for some unknown function $B^*(k)$, where the requirement (2.19*c*) that $\tau \to 0$ as $z \to \infty$ implies that $\tau^* \to 0$ as $|\zeta| \to \infty$ and hence that the argument of ζ lies in the range $(-\pi/3, \pi/3)$. Thus the k-plane has a branch-cut along the positive imaginary axis.

Substitution of (3.1) into the boundary and matching conditions (2.19*b*) and (2.19*e*) and elimination of the unknown function $B^*(k)$ allows us to express the transform of the pressure variable in terms of that of the core streamline perturbation:

$$P^* = \frac{\gamma}{(\mathrm{i}k)^{1/3}} A^*, \tag{3.2}$$

where the positive constant γ takes the value $-18 \times 6^{2/3}\mathrm{Ai}'(0)$; Ai′ is the derivative of Ai.

A further pair of equations may be obtained from the lower boundary-layer equations and conditions (2.20):

$$\tilde{P}^* = \frac{-\gamma}{(\mathrm{i}k)^{1/3}}(A^* + F^*), \tag{3.3}$$

and from the pressure relation (2.21) we have

$$P^* = \tilde{P}^* - \sigma k^2 A^*. \tag{3.4}$$

Eliminating the transforms of the pressures P^* and $\tilde{P}^*$ from (3.2)–(3.4) and inverting the Fourier transform, we obtain an expression for the core streamline displacement in terms of the membrane displacement:

$$A(x) = G(x) \star F(x), \tag{3.5}$$

where the function $G(x)$ has Fourier transform $G^*(k) = -\frac{1}{2}(1+\sigma k^2(\mathrm{i}k)^{1/3}/2\gamma)^{-1}$ and $\star$ represents a convolution.

Further manipulation of these three equations leads to expressions for the two pressure distributions,

$$P = \frac{\sigma A_{xx} - G_1 \star F}{2}, \tag{3.6a}$$

$$\tilde{P} = \frac{-\sigma A_{xx} - G_1 \star F}{2}, \tag{3.6b}$$

and for the wall-shear perturbations,

$$\tau(x,0) = -18(6)^{1/3}\mathrm{Ai}(0)G_2(x) \star A(x), \tag{3.7a}$$

$$\tilde{\tau}(x,0) = 18(6)^{1/3}\mathrm{Ai}(0)G_2(x) \star (F(x) + A(x)), \tag{3.7b}$$

where the functions $G_1(x)$ and $G_2(x)$ have Fourier transforms

$$G_1^*(k) = \gamma/(\mathrm{i}k)^{1/3} \quad \text{and} \quad G_2^*(k) = (\mathrm{i}k)^{1/3},$$

respectively.

When solving the full membrane problem we must couple the membrane equation (2.22) to the convolution integrals (3.5)–(3.7). The convolving functions are

$$G(x) = \begin{cases} -\dfrac{3}{14}\beta \mathrm{e}^{\beta x} & \text{for } x < 0, \\ \dfrac{3\beta}{7}\mathrm{e}^{\beta x c}\sin\left(\beta x s - \dfrac{9\pi}{14}\right) + \dfrac{\sqrt{3}}{4\pi}\displaystyle\int_0^\infty \frac{R\mathrm{e}^{-rx}}{1-R+R^2}\,\mathrm{d}r, & \text{for } x > 0, \end{cases} \tag{3.8a}$$

$$G_1(x) = \begin{cases} 0 & x < 0, \\ \dfrac{\sqrt{3}\gamma\Gamma(2/3)}{2\pi x^{2/3}} & x > 0, \end{cases} \tag{3.8b}$$

$$G_2(x) = \begin{cases} 0 & x < 0, \\ \dfrac{\sqrt{3}\Gamma(4/3)}{2\pi x^{4/3}} & x > 0, \end{cases} \tag{3.8c}$$

where

$$\beta = \left(\frac{2\gamma}{\sigma}\right)^{3/7}, \qquad R = \frac{\sigma}{2\gamma}r^{7/3}, \qquad s = \sin(6\pi/7), \qquad c = \cos(6\pi/7).$$

These are obtained by taking inverse Fourier transforms of $G^*(k)$, $G_1^*(k)$ and $G_2^*(k)$ respectively.

If $P_{ext} \neq 0$, we see that, in any solution found, the various functions will be proportional to the external pressure; it is therefore sufficient to consider the two cases $P_{ext} = 0$ and $P_{ext} \neq 0$. We note that in the case of zero cross-stream pressure gradient, where there is no perturbation to the flow upstream of the membrane, these correspond to zero and non-zero transmural pressure at the upstream end of the membrane.

3.2. *Non-zero upstream transmural pressure*

3.2.1. *Asymptotically high tension*

For large T the membrane equation (2.22) suggests the scaling $h = T^{-1}$. To leading order in T^{-1} the membrane shape is then independent of the flow, and we may construct an analytic solution as an asymptotic expansion in powers of T^{-1},

$$(F, A, P, \tilde{P}, \tau, \tilde{\tau}) = (F_0, A_0, P_0, \tilde{P}_0, \tau_0, \tilde{\tau}_0) + T^{-1}(F_1, A_1, P_1, \tilde{P}_1, \tau_1, \tilde{\tau}_1) + O(T^{-2}),$$

for which the membrane and flow equations decouple at each order. The leading-order membrane shape is quadratic,

$$F_0 = \begin{cases} \frac{1}{2} P_{ext} x(1-x) & \text{for } x \in (0,1), \\ 0 & \text{for } x \notin (0,1), \end{cases} \tag{3.9}$$

and allows us to find the leading-order approximations for the flow variables A_0, P_0, $\tilde{P}_0$, τ_0 and $\tilde{\tau}_0$. Since the expressions obtained are long and unilluminating, they are not reproduced here; instead the various functions are plotted in figure 2, in which the effect of varying σ is shown.

When $\sigma = 0$, there is no upstream influence exerted on the flow by the membrane deformation $A_0 = -F_0/2$, as expected (see e.g. Smith 1976*a*), while the pressure and wall-shear perturbation distributions are the same in the two boundary layers. We see that the region of adverse pressure gradient and negative wall-shear perturbation lies around the downstream end of the membrane, indicative of a tendency towards separation, in both boundary layers, at this position.

As the cross-stream pressure gradient is increased, the amount of upstream influence, visible in all these functions, increases. The core streamline displacement decreases in amplitude, increases in streamwise extent and overshoots downstream before returning to zero. For larger σ the amplitude of the pressure and wall-shear perturbations are decreased/increased on the upper (i.e. rigid)/lower boundaries. In particular, the results suggest that the tendency towards reversed flow at the downstream end of the membrane is decreased/increased in the upper/lower boundary layer as σ increases and is absent altogether in the upper boundary layer for sufficiently large σ.

The region around the upstream end of the membrane in the lower boundary layer also develops an adverse pressure gradient and negative wall-shear perturbation as σ increases, suggesting that a secondary, weaker, region of reversed flow may develop there at larger amplitude. The upstream separation for large indentations was analysed by Smith (1977) and Smith & Duck (1980).

Given the leading-order pressure distribution in the lower boundary layer, $\tilde{P}_0$, we may now evaluate the first correction to the membrane shape caused by this flow. Again, the function obtained is lengthy but is plotted for various values of σ in figure 3. As σ increases and causes the reduction in pressure through the constriction to be confined more and more to the lower boundary layer, the reduction in $\tilde{P}_0$ (figure 2*b*) leads to a greater deformation in the membrane.

3.2.2. *Extension to moderate values of T*

We eliminate A and $\tilde{P}$ from (2.22), (3.5) and (3.6*b*) and integrate twice to produce an integral equation for F,

$$TF(x) = \begin{cases} \dfrac{\mathscr{G}(x) \star F(x)}{2} - \dfrac{P_{ext} x^2}{2h} + T(ax + b) & \text{for } x \in (0,1), \\ 0 & \text{for } x \notin (0,1), \end{cases} \tag{3.10}$$

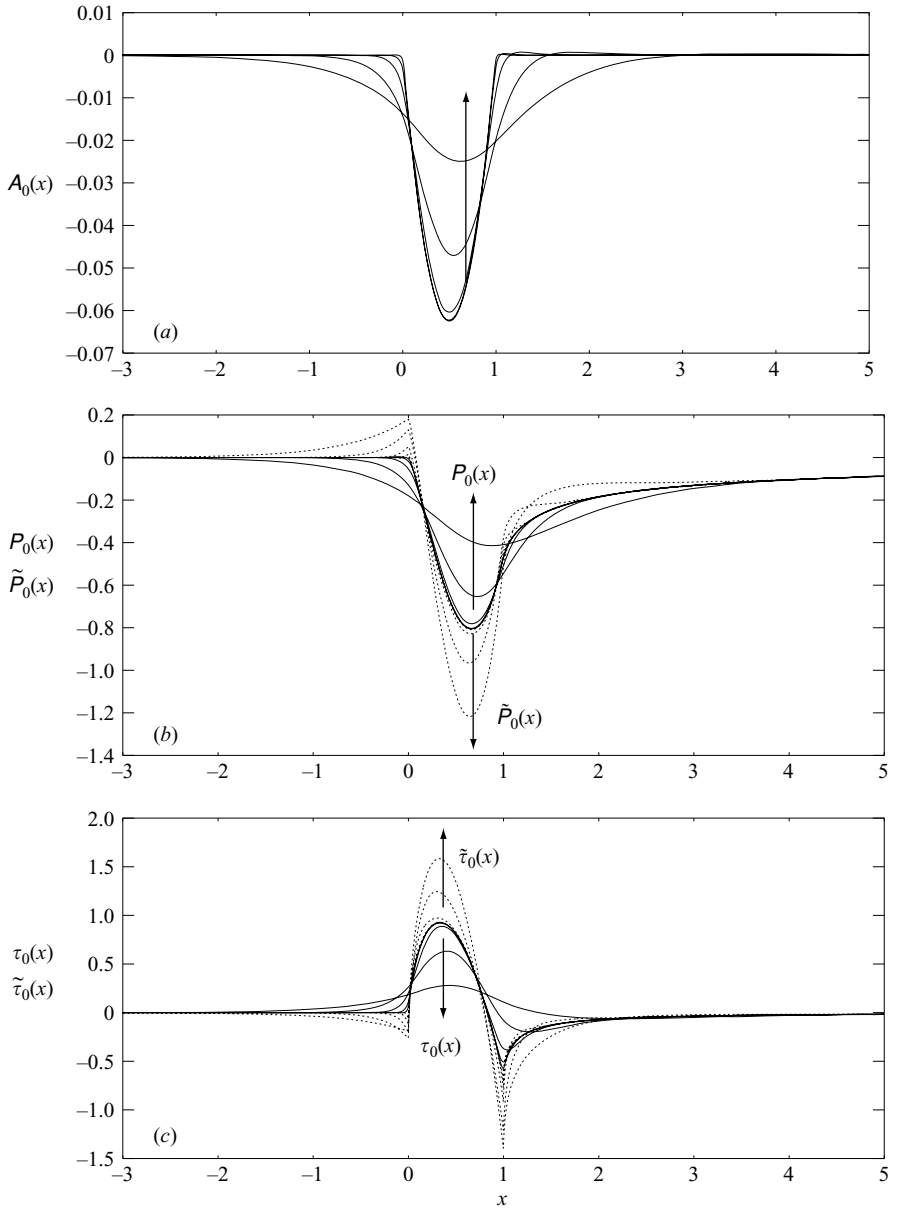

FIGURE 2. Leading-order functions calculated in the limit of large tension: (*a*) core streamline perturbation function A_0; (*b*) pressure distributions P_0 and $\tilde{P}_0$; (*c*) Wall shear stresses in the two boundary layers τ_0 and $\tilde{\tau}_0$, where the solid (dashed) lines give results for the upper (lower) boundary layer respectively, calculated for $\sigma = 0.001, 0.01, 0.1, 1, 10$ and $P_{ext} = 1$. Each arrow indicates the direction of increasing σ.

where $\mathscr{G}(x) = -\sigma G(x) - \int^x \int^{x'} G_1(x'')\,\mathrm{d}x''\,\mathrm{d}x'$, $G(x)$ and $G_1(x)$ are given in (3.8), a and b are constants of integration chosen to satisfy $F(0) = F(1) = 0$ and $\star$ represents a convolution.

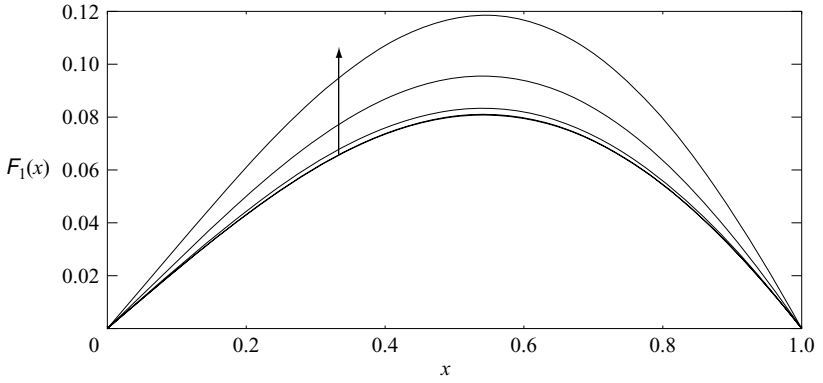

FIGURE 3. First correction F_1 to wall shape, for $\sigma = 0.001, 0.01, 0.1, 1, 10$. The arrow indicates the direction of increasing σ. Note that the curves for the two smallest values of σ are almost indistinguishable.

The iteration

$$f_{n+1}(x) = \begin{cases} \dfrac{\mathscr{G}(x) \star f_n(x)}{2T} - \dfrac{P_{ext}x^2}{2hT} + a_n x + b_n & \text{for } x \in (0,1), \\ 0 & \text{for } x \notin (0,1), \end{cases} \tag{3.11}$$

where the constants a_n and b_n are determined by the requirement that f_{n+1} be zero at $x = 0, 1$, gives an equivalent method to that used in the previous section to find the asymptotic solution: setting $f_{-1} = 0$, we recover

$$f_0(x) = F_0(x), \tag{3.12a}$$

$$f_1(x) = F_0(x) + \frac{1}{T}F_1(x), \tag{3.12b}$$

etc. The iteration may thus be expected to converge for sufficiently large values of T and may be regarded as an extension of the analytic solution to more moderate tensions.

Data resulting from the numerical solution of (3.11) are plotted with $P_{ext} = 1$ (without loss of generality because the problem is linear) in figure 4. Since the shape of the membrane remains unimodal it is characterized at each value of the tension by F_{max}, the value of F at the point of maximum deflection. As the tension is reduced, the size of the deformation increases until a value T_c is approached where F_{max} becomes very large and below which the iteration ceases to converge. As shown in figure 4, this behaviour is fitted empirically by $F_{max} = c/(T - T_c)$, suggesting a singularity in the solution of the steady linearized problem at a finite value of $T_c \approx 0.609$. This will be shown later (§ 4.2) to be the result of the failure of the linearized problem to capture a turning point in the solution branch.

3.3. *Zero upstream transmural pressure*

If the transmural pressure at the upstream end of the membrane is zero then the trivial solution of no membrane deformation and undisturbed Poiseuille flow throughout the channel, i.e. $F = A = P = \tilde{P} = V = \tilde{V} = 0$, $U = 6z$, $\tilde{U} = 6\tilde{z}$, solves the nonlinear boundary-layer problem given by (2.11)–(2.15) and (2.17) for all values of the tension T and the cross-stream pressure-gradient parameter σ. However, non-trivial solutions are possible for certain values of T.

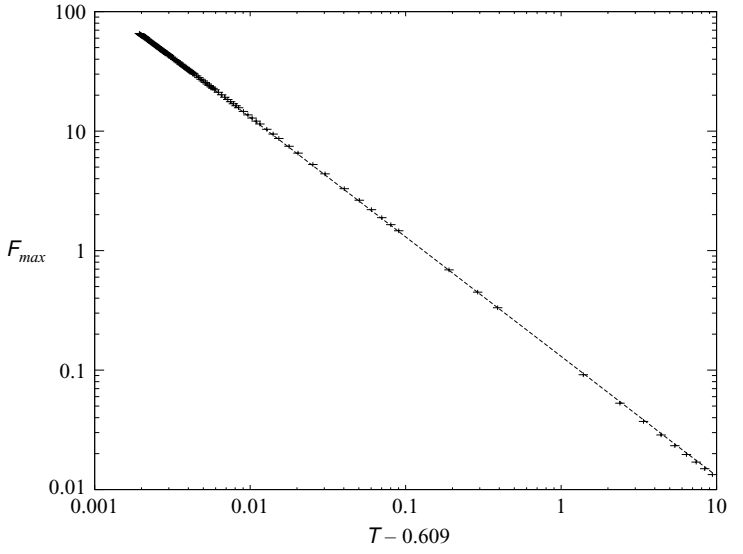

FIGURE 4. Log log plot of $T - T_c$ against F_{max} in the case $\sigma = 0$, $P_{ext} = 1$, found by numerical solution of the iteration relation, showing data points fitted by the line $c/(T - T_c)$; $T_c \approx 0.609$.

We expand the membrane deformation F as a half-range Fourier series,

$$F(x) = \begin{cases} \displaystyle\sum_{n=1}^{\infty} f_n \sin n\pi x, & x \in (0, 1), \\ 0 & \text{elsewhere}, \end{cases} \tag{3.13}$$

and show that the two expressions for $\tilde{P}$ deriving from the membrane equation (2.22) and the flow equations (3.3) and (3.5) lead to an infinite set of nontrivial eigensolutions.

3.3.1. *Negligible cross-stream pressure gradient*

When σ is zero, $A = -F/2$, as has previously been observed. The convolution expression (3.3) for $\tilde{P}$ thus yields

$$\tilde{P} = -\frac{\gamma}{4\pi} \int_{-\infty}^{\infty} \frac{\mathrm{e}^{\mathrm{i}kx} F^*(k)}{(\mathrm{i}k)^{1/3}} \mathrm{d}k, \tag{3.14}$$

upon inversion of the Fourier transform; evaluating the transform of the Fourier series expression (3.13) for $F(x)$ this becomes

$$\tilde{P} = -\frac{\gamma}{2} \sum_{m=1}^{\infty} \frac{f_m}{(m\pi)^{1/3}} \left(\sin(m\pi x - \pi/6) + \frac{\sqrt{3}}{2\pi} \int_0^{\infty} \frac{\mathrm{e}^{-m\pi x r}}{r^{1/3}(1 + r^2)} \, \mathrm{d}r \right).$$

Expressing the terms in the parentheses as a Fourier series we thus obtain our first Fourier series expression for $\tilde{P}$:

$$\tilde{P} = -\frac{\gamma}{2} \sum_{n=1}^{\infty} \sum_{m=1}^{\infty} \frac{f_m}{(m\pi)^{1/3}} b_{mn} \sin n\pi x, \tag{3.15}$$

where

$$b_{mn} = \begin{cases} \dfrac{n((-1)^{n+m}-1)}{\pi(n^2-m^2)} + \dfrac{\sqrt{3}n}{\pi^2}\displaystyle\int_0^\infty \frac{(1-(-1)^n \mathrm{e}^{-m\pi r})}{r^{1/3}(1+r^2)(m^2r^2+n^2)}\,\mathrm{d}r & \text{for } m \neq n, \\ \dfrac{\sqrt{3}}{2} + \dfrac{\sqrt{3}n}{\pi^2}\displaystyle\int_0^\infty \frac{(1-(-1)^n \mathrm{e}^{-m\pi r})}{r^{1/3}(1+r^2)(m^2r^2+n^2)}\,\mathrm{d}r & \text{for } m = n. \end{cases} \tag{3.16}$$

Another expansion is obtained directly from the membrane equation:

$$\tilde{P} = -T\sum_{n=1}^{\infty} n^2\pi^2 f_n \sin n\pi x \quad \text{for } x \in (0,1), \tag{3.17}$$

and, equating the coefficients of $\sin n\pi x$ between these two Fourier series, we have

$$T\boldsymbol{f} = \mathscr{B}\boldsymbol{f}, \tag{3.18}$$

where the vector $\boldsymbol{f}$ is formed from the Fourier coefficients f_n, and the non-symmetric matrix $\mathscr{B}$ has entries

$$(\mathscr{B})_{nm} = \frac{\gamma}{2n^2\pi^{7/3}m^{1/3}} b_{mn}.$$

We have thus derived an eigenvalue problem, in which non-trivial eigensolutions of the linearized problem exist at a discrete set of values T_i and are described by the vector of their Fourier coefficients $\boldsymbol{f}_i$, where $T_i\boldsymbol{f}_i = \mathscr{B}\boldsymbol{f}_i$.

The values of the T_i are found numerically by considering the eigenvalues of the truncated matrices $\mathscr{B}_N$, with entries B_{mn} for $1 \leqslant m, n \leqslant N$, where N increases from 2 to 100. As N increases the number of real eigenvalues seen increases; each converges rapidly to its final value once it has appeared. The converged values produced by this method give a sequence $T_1 > T_2 > T_3 > \cdots > 0$ of eigenvalues, listed in order of appearance as N increases.

This suggests that (3.18) has an infinite decreasing series of real positive eigenvalues. As the tension decreases, the eigenvalues correspond to higher-mode membrane shapes. More specifically, the eigenvalue T_i corresponds to a membrane shape with i extrema.

3.3.2. *Non-zero cross-stream pressure gradient*

The results for $\sigma \neq 0$ can be derived in a manner similar to the above. We must now use the convolution relation (3.5) to obtain the core streamline perturbation in terms of F, so (3.14) becomes

$$\begin{aligned} \tilde{P} &= \frac{1}{2\pi}\int_{-\infty}^{\infty} \frac{-\gamma \mathrm{e}^{\mathrm{i}kx}}{(\mathrm{i}k)^{1/3}}(G^*(k)+1)F^*(k)\,\mathrm{d}k, \\ &= 2G(x) \star \tilde{P}_{\sigma=0}(x) + 2\tilde{P}_{\sigma=0}(x), \end{aligned} \tag{3.19}$$

where $\tilde{P}_{\sigma=0}(x)$ denotes the solution found the case of negligible cross-stream pressure gradient (3.15) and $G(x)$ is given by (3.8*a*). As before, we express this as a Fourier series and equate coefficients of $\sin n\pi x$ with those in the alternative series (3.17) derived from the membrane equation, to obtain an infinite eigenvalue problem.

The eigenvalues are again evaluated numerically, the results being shown for a range of σ and T in figure 5. As σ is increased, pairs of eigenvalues approach and vanish, starting with those at the smallest values of T, until finally the pair T_1, T_2 disappears at $\sigma \approx 2.2$. There is then a range of σ where there are no real eigenvalues until further solution branches start to appear at $\sigma \approx 40$. These large-σ branches,

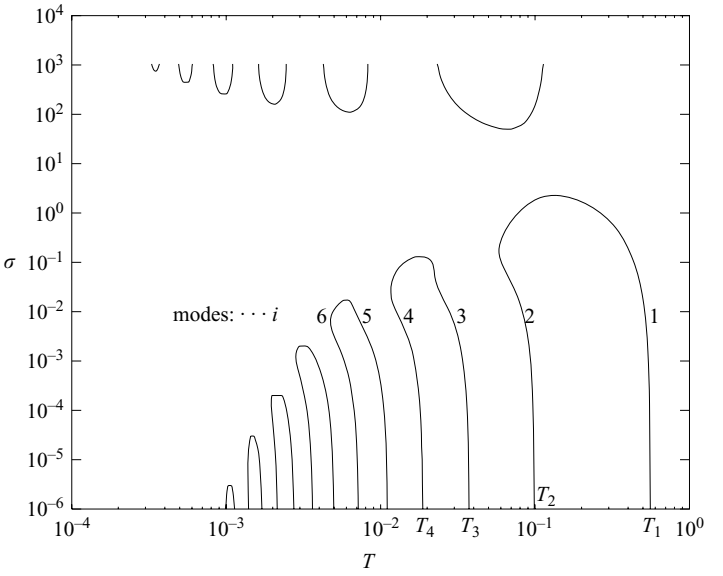

FIGURE 5. The real eigenvalues T_i of the linearized problem shown as σ varies and calculated for the matrix equation truncated at $N = 100$. The rightmost curve at each σ gives the unimodal eigensolution corresponding to T_1, values of i are marked and it can be seen that i increases to the left.

however, invalidate the assumption $\sigma = O(1)$ made in establishing the boundary-layer formulation and are unlikely to be physically meaningful. They will not be discussed further.

4. Numerical solution of the nonlinear problem

4.1. *Numerical methods*

We use a Keller-box discretization, in which the boundary-layer equations, e.g., (2.11)–(2.14) are reduced to a set of first-order differential equations by the introduction of supplementary functions, and a second-order centred-difference scheme is constructed; see Keller (1971, 1978).

4.1.1. *Solution method when* $\sigma = 0$

When there is no cross-stream pressure gradient, the core streamline displacement is simply given by half the membrane displacement, $A = -F/2$, and the problem reduces to the coupling of the flow in a single boundary layer to the displacement of the membrane.

The lack of upstream influence means that the flow remains undisturbed until the start of the membrane at $x = 0$, where there is a discontinuity in the wall slope, $F'(x)$. The effect of this corner is then felt by a sublayer which grows as $x^{1/3}$ downstream (Smith 1976*a*) indicating the need for either a change of variables to capture this behaviour or for a smaller step size in the region near the corner.

There is no upstream influence, so in cases where there is no flow reversal the boundary-layer flow over a given wall shape is determined by the upstream conditions and may be found by marching forwards from $x = 0$. This idea can be extended: by specifying the slope of the membrane at its upstream end in addition to requiring that the displacement be zero there we may determine the evolution downstream of

the coupled fluid–structure problem and, in particular, the consequent value of F at $x = 1$. The condition that the displacement of the membrane is zero at its downstream end is then satisfied by a shooting algorithm in which the initial slope is varied until $F(x = 1) = 0$.

This procedure assumes that the downstream velocity component, U, remains positive over the entire domain or that the regions of reversed flow are sufficiently small and weak that the resulting numerical instability leads only to small errors in the solution. The FLARE approximation (Reyhmer & Flügge-Lotz 1968), in which the advection of momentum in the reverse direction is neglected by setting uu_x to zero whenever its value is negative, was also used to examine its effect upon the results produced. Since it appears to make little quantitative and no qualitative difference to the results we conclude that the errors arising from the regions of reversed flow are not significant.

Our code was tested by verifying quadratic convergence and confirming that the results at high tension and at zero upstream transmural pressure agree with those obtained from the linearized analyses. Figure 6 shows results spanning the range of parameter values for which the code was employed; the regions of parameter space in which reversed flow was produced are shown. This demonstrates the parameter ranges over which the code works.

4.1.2. *Solution method when* $\sigma \neq 0$

The addition of a cross-stream pressure gradient to the problem means that we must now solve the full, coupled, pair of boundary-layer problems over a domain extending sufficiently far up- and downstream that it includes the entire disturbed region. The interaction between the membrane displacement and the core streamline perturbation means that a marching algorithm is no longer feasible; instead the problem is solved directly using Newton's method over the entire domain. The results were verified by comparison of the solutions obtained as $\sigma \to 0$ with those obtained from the marching method at $\sigma = 0$ (which were also repeated using a direct solver).

4.2. *Results when* $\sigma = 0$

The shooting method described in § 4.1.1 was used to perform a parameter study over a range of values of the external pressure and tension, taking the internal pressure at the upstream end of the membrane to be zero, in order to discover which values of the initial slope of the membrane correspond to steady solutions of the problem. These calculations were then repeated using the direct solution method described in § 4.1.2.

From the results found in this study, a series of bifurcation diagrams in $(F_x(0), T)$-space was constructed, each at a particular value of the external pressure P_{ext} (figure 6), where $F_x(0)$ is the slope of the membrane at its upstream end and T is the tension. Solutions for which the flow is entirely forwards are plotted with a solid line, while those for which a portion of the flow was found to be reversed are plotted with a dashed line.

We discuss now the existence and shape of steady solutions as the upstream transmural pressure P_{ext} ranges from a large positive to a large negative value.

4.2.1. *Large positive upstream transmural pressure*

When P_{ext} is large and positive (figure 6*a*), numerical solution of the nonlinear boundary-layer equations reveals only one branch of solutions. This reaches a minimum value of the tension at its turning point, $(T^c, F_x(0)^c)$, which is given by (1.9), (5.8) to one decimal place for $P_{ext} = 10$ (figure 6*a*) and is asymptotic to the

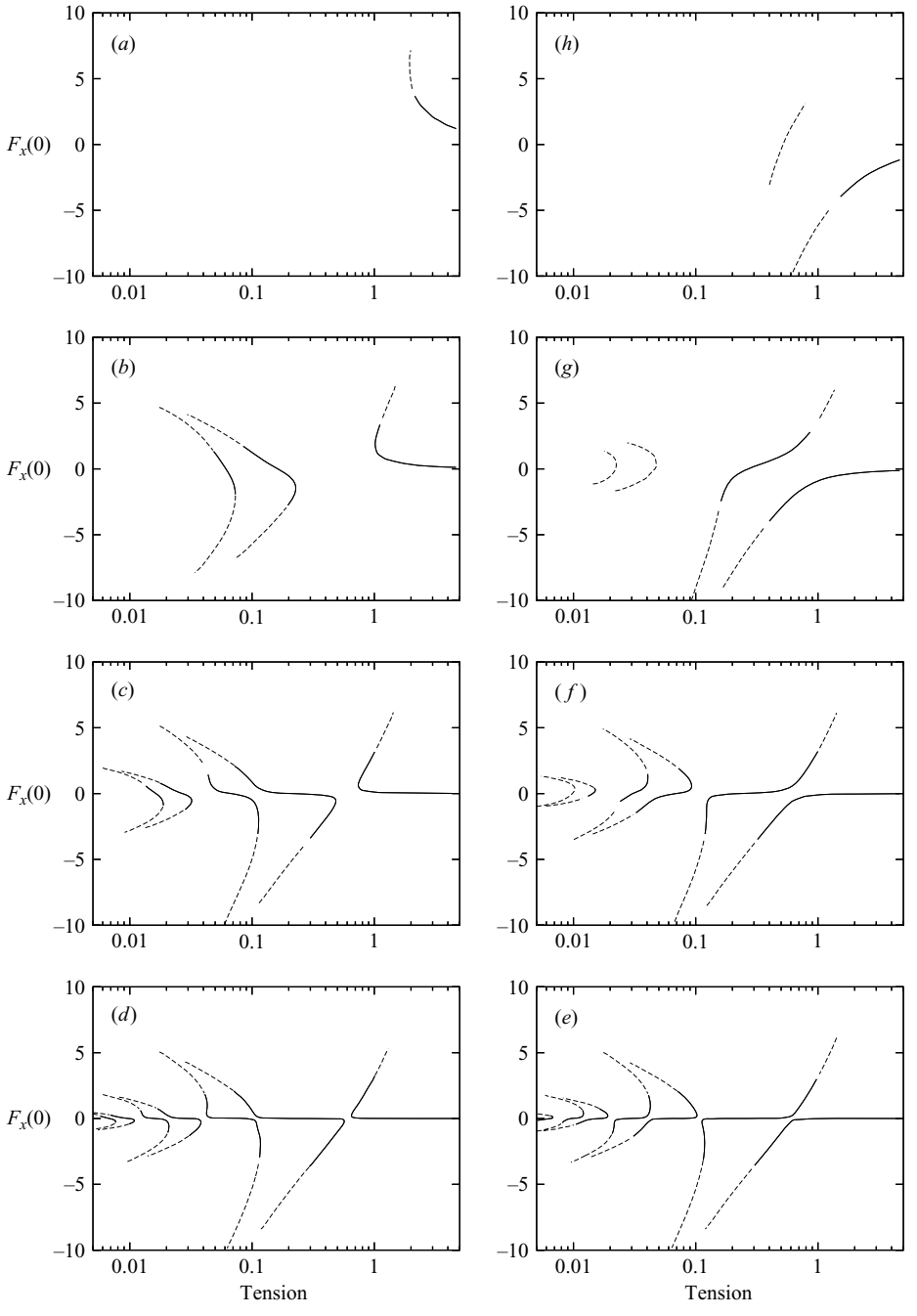

FIGURE 6. Bifurcation diagrams with $\sigma = 0$ for (*a*) $P_{ext} = 10$, (*b*) $P_{ext} = 1$, (*c*) $P_{ext} = 0.1$, (*d*) $P_{ext} = 0.01$, (*e*) $P_{ext} = -0.01$, (*f*) $P_{ext} = -0.1$, (*g*) $P_{ext} = -1$ and (h)$P_{ext} = -10$, each to the same scale. The membrane slope at the upstream end is plotted against the non-dimensional tension. The dashed curves indicate solutions in which there are regions of flow reversal.

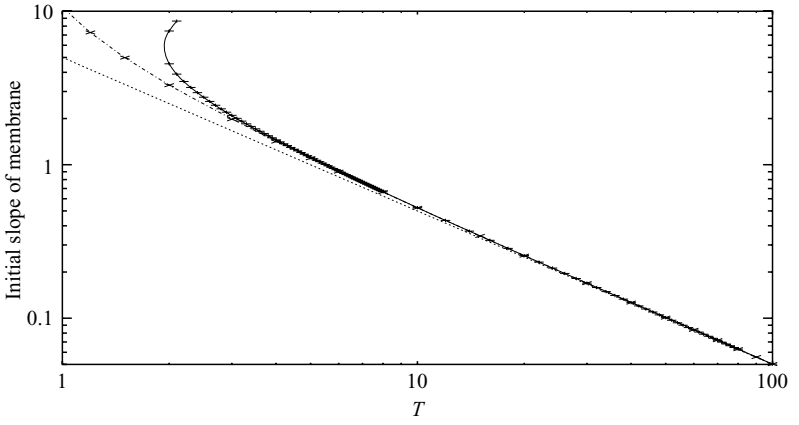

FIGURE 7. The initial slope of the membrane plotted against the tension in the membrane for $P_{ext} = 10$. The results calculated via the high-tension asymptotic limit (dashed line) may be compared with those calculated via the iterative method for the linearized equations (dot-dashed line) and the numerical solution of the nonlinear boundary-layer equations (solid line). The iterative and numerical solutions are shown with curves fitted through the calculated points.

axis $F_x(0) = 0$ as T becomes large. There is thus a minimum value of the tension at which a steady solution exists. Figure 10 shows the region of (T, P_{ext})-space in which steady solutions exist.

The lower part of the branch in figure 6(a), for which $F_x(0) < F_x(0)^c$, corresponds to the continuation of the solution found in analytic form in the limit of asymptotically large tension in § 3.2.1 and then extended down to moderate values of the tension in § 3.2.2. Figure 7 shows for comparison the relation between the tension in the membrane and the slope adopted at its upstream end found using the three different methods discussed, which are as follows.

Asymptotic limit Here we evaluate the initial slope of the membrane by taking the derivative of the expression (3.9) for the membrane shape, which was obtained by assuming that the deformation is sufficiently small that the problem may be linearized and that the tension is sufficiently high that the membrane behaviour is decoupled from the flow at leading order. This gives $\partial F/\partial x = P_{ext}/2T$ at $x = 0$ and is shown by the dashed (lowest) line in figure 7.

Integral equation The asymptotic solution of the linearized boundary-layer equations is extended to moderate values of the tension via the iterative form of the integral equation, as described in § 3.2.2. The results of this process are shown by the dot-dashed (middle) curve in figure 7.

Numerical solution The nonlinear boundary-layer equations are solved numerically; see the solid (top) curve in figure 7. As expected, for sufficiently high tension (i.e. for values of T above 20 or so), the results from the three methods are in good agreement. Regarding the numerical solution as the most accurate, the integral-equation results do indeed give an improvement over the asymptotic limit, remaining in agreement with the numerical results down to a tension of 4 or 3; below this the two curves diverge as the solution derived from the linearized set of equations fails to capture the turning point exhibited by the numerical results from the nonlinear equations.

Our understanding of the small-tension behaviour has thus improved from an expectation of a solution for all values of T (the asymptotic limit applied for arbitrary T) through an apparent singularity at some finite value of the tension, as discussed

in § 3.2.2, to an appreciation from the solution of the nonlinear boundary-layer equations of the fact that this solution branch has a turning point at a finite value of the tension.

The upper part of the branch found by solution of the nonlinear boundary-layer equations, for which $F_x(0) > F_x(0)^c$, describes more highly collapsed solutions than the lower, as shown by the inserts in figure 8. As the branch is followed round from the lower part to the upper the solution deforms continuously, and we start to see regions of reversed flow once the value of the initial slope becomes sufficiently large. When $P_{ext} = 10$ the last point found on the lower section of the branch marks the onset of flow reversal; for the smaller values of the external pressure shown, the membrane is not sufficiently deformed on the lower section of curve to cause the flow to reverse. The onset of reversal is thus postponed until some distance along the upper part of the branch (figures 6*a*, *b*).

4.2.2. *Upstream transmural pressure decreasing towards zero*

As the positive external pressure is decreased towards zero, additional solution branches appear at lower values of the tension (figures 6*b–d*), which correspond to higher-mode solutions of the system (figure 8). Since the amplitude of the membrane deformation increases towards the downstream end, as may be seen in the insets on the left of figure 8, the value of the maximum of $F(x)$ increases more rapidly with $F_x(0)$ for higher-mode branches. This means that reversal occurs at a smaller value of $|F_x(0)|$ as successively higher-mode branches are considered, as may be seen in figure 6.

Each branch appears initially as a small loop of solutions; as P_{ext} is gradually decreased these spread to produce the apparently open branches shown in figure 6(*b*). The emergence and initial spreading of the first branch as P_{ext} is reduced from 1.9 to 1.7 is shown in figure 9(*a*) and the appearance of the second as the first continues to spread in figure 9(*b*). The two branches initially appear at slightly different values of P_{ext} and T, the first at $(P_{ext}, T, F_x(0)) \approx (1.83, 0.055, -0.5)$ and then the second at $(P_{ext}, T, F_x(0)) \approx (1.59, 0.028, -0.5)$. Since the code does not converge for large values of $|F_x(0)|$ or for very small values of T, the behaviour of some sections of branches in these regions is not known.

Typical shapes assumed by the membrane on each of the branches present when $P_{ext} = 1$ are seen in the inserts in figure 8. These are all plotted on the same axes, x ranging from 0 to 1 on the abscissa and F ranging from -2.5 to 5 on the ordinate. Each shows:

(i) the membrane shape

(ii) the streamlines, the same values of the stream function being plotted in each insert; those illustrating distended regions of the membrane each show some degree of flow reversal; in no case has the numerical instability grown large enough to be visible

(iii) the contours of dissipation; the dissipation is reduced in distended regions and increased over collapsed regions

The qualitative form of the membrane shape adopted by any given solution may be described in terms of the number and order of the local maxima and minima of the function $F(x)$. As any given branch is followed from negative values of $F_x(0)$ to positive, we either gain an additional local maximum or lose a local minimum as $F_x(0)$ passes through zero. The mode of the membrane shape thus either increases or decreases by unity, depending upon the sign of the upstream transmural pressure, $P_{ext} - \tilde{P}(0) = P_{ext}$, and thus upon the sign of the curvature of the membrane at

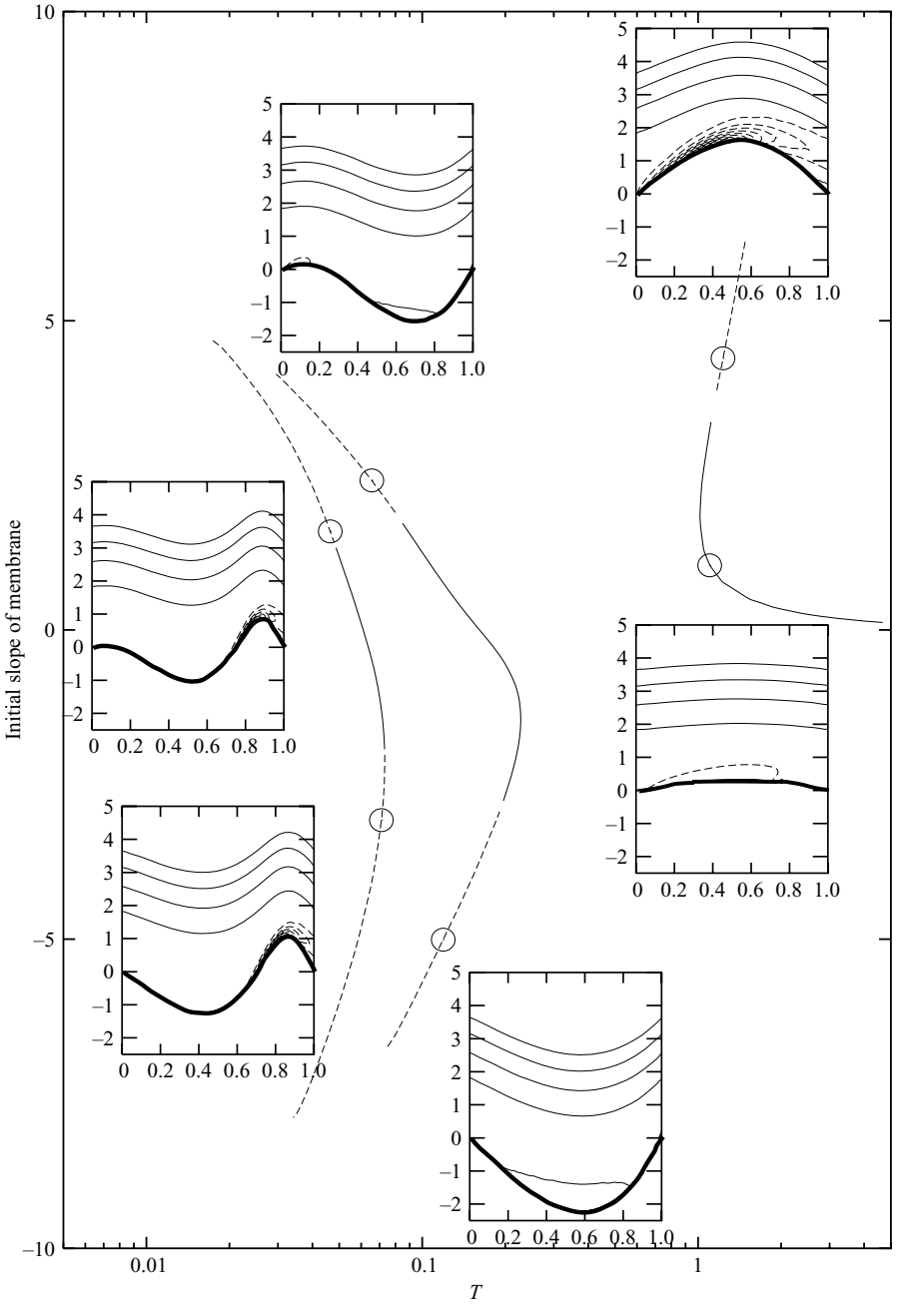

FIGURE 8. Solutions for $P_{ext} = 1$. The main figure is a larger version of figure 6(*b*). The inserts are all plotted on the same scale, showing the solutions calculated at the points indicated by circles. Each insert shows the membrane shape, a few streamlines and some contours of dissipation (dashed lines). Note the regions of reversed flow in two cases where the membrane bulges out (top left and bottom).

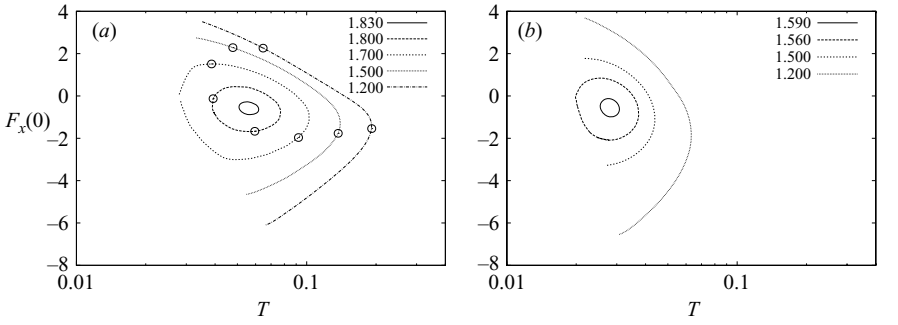

FIGURE 9. Bifurcations at which the first pair of low-tension branches appear. Data plotted for (*a*) branch 1, $P_{ext} = 1.83, 1.8, 1.7, 1.5$ and 1.2 and (*b*) branch 2, $P_{ext} = 1.59, 1.56, 1.5$ and 1.2. No solutions were found in this range of tension for $P_{ext} \geqslant 1.85$. The circles in (*a*) indicate solutions with downstream transmural pressure of -1.

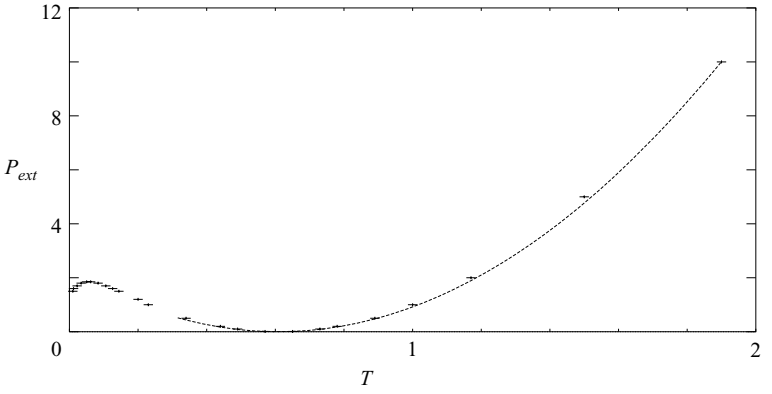

FIGURE 10. The boundary in the (P_{ext}, T)-plane between parameter values for which a solution exists and those for which it does not. The points plotted are extracted from the numerical data, while the curve shows part of the function $6(T^c - 0.60859)^2$, where $T = 0.60859$ is the value of the first global bifurcation point, as shown in figure 11.

its upstream end. The downstream end of the membrane, however, remains either collapsed or dilated over the whole of the solution branch.

The mode of the solution adopted increases as branches at smaller and smaller tension are considered. Hence, as P_{ext} is reduced towards zero, branches corresponding to successively higher-mode solutions appear.

For all positive P_{ext} there is a range of tensions for which no steady solutions exist. The evolution of this region as the upstream transmural pressure decreases towards zero is plotted in figure 10, in which the local maximum at small values of the tension shows the appearance of the first low-tension branch. From this we see that the values of (T^c, P^c_{ext}) to the right of the minimum at $T \approx 0.6$, i.e. the turning points of the high-tension branch of solutions (figure 6*a*), are well fitted empirically by the function $P^c_{ext} = 6(T^c - T_1)^2$, where T_1 is the tension at the first global bifurcation point.

4.2.3. *Zero upstream transmural pressure*

When the upstream transmural pressure is zero, the trivial solution is valid for all values of the tension. The presence of this line of solutions may be inferred from figure 6 by the fact that the deformation of the solution branches tends to form a line

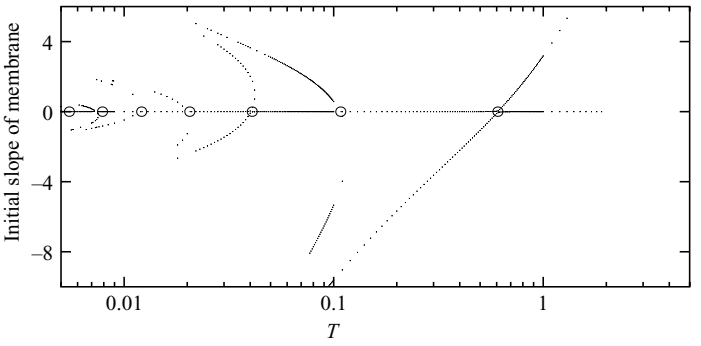

FIGURE 11. Bifurcation diagram plotted for $P_{ext} = 0$ (dots) plus eigenvalues calculated from the search for non-trivial Fourier series solutions of the linearized problem (circles).

along $F_x(0) = 0$ as the value of P_{ext} tends towards zero from either above or below, with a series of simultaneous global bifurcations at points T_i along the axis $F_x(0) = 0$, where pairs of branches collide.

These T_i thus give the small-deformation limit of the non-trivial solutions present when $P_{ext} = 0$ and hence correspond to the eigenvalues found when seeking non-trivial Fourier-series solutions to the linearized system of equations in the case when $P_{ext} = 0$, discussed in § 3.3. Figure 11 shows the eigenvalues found in § 3.3, given by the circles marked along the $F_x(0) = 0$ axis, and the bifurcation diagram plotted for $P_{ext} = 0$ from the numerical solution of the nonlinear boundary-layer equations. The positions of the eigenvalues compare well with the positions of the global bifurcation points.

The modes of the solutions predicted on the various solution branches by the Fourier-series analysis of the linearized system of equations are seen to agree with those produced by the numerical solution of the nonlinear boundary-layer equation.

4.2.4. *Negative upstream transmural pressure*

When P_{ext} is further reduced below zero, the connection between the branches is seen to alter at each of the global bifurcation points (compare figures 6*d* and 6*e*, which give the diagrams for $P_{ext} = 0.01$ and -0.01 respectively), so that the bifurcation diagram has a qualitatively different structure depending upon whether the upstream transmural pressure is positive or negative.

As the magnitude of P_{ext} increases, the solution branches continue to deform and vanish (figures 6*e–h*), starting with those corresponding to higher modes, until just two solution branches remain (figure 6*h*) at large negative values of P_{ext}. It appears that steady solutions exist for all values of the tension although the deformation becomes too large to be captured by the methods used here over some ranges of the tension. We note in particular that unimodal collapsed solutions exist for all values of the upstream transmural pressure, for T sufficiently large.

4.3. *Results when* $\sigma \neq 0$

When the cross-stream pressure gradient is not negligible, the coupled boundary-layer problem must be solved using a direct method of solution over a sufficiently long domain that the flow at the up- and downstream ends is undisturbed.

The effect of the cross-stream pressure gradient on the flow is shown in figure 12, in which a comparison between the streamlines and dissipation contours when $\sigma = 0.01$ and $\sigma = 1$ is shown. The results are plotted for both the top and bottom boundary

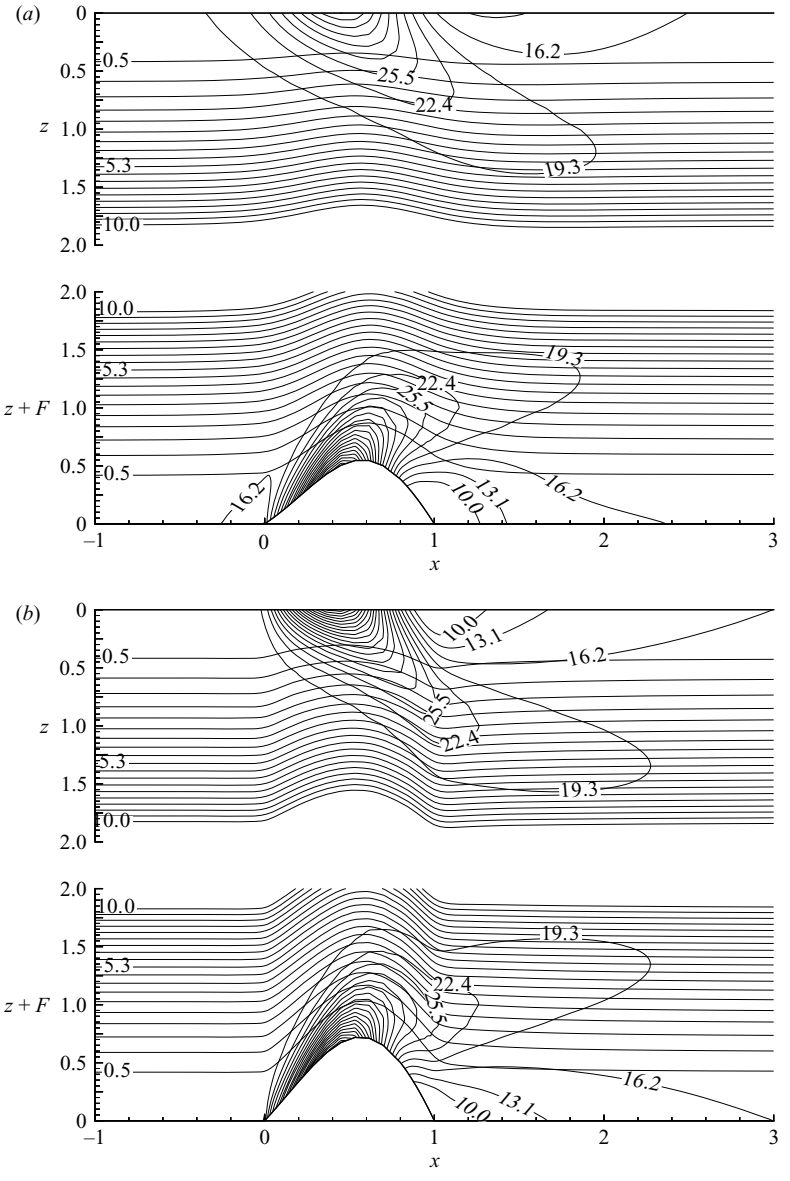

FIGURE 12. Streamline and dissipation contours for the two boundary layers when $P_{ext} = -1.0$, $T = 0.63733$ and (*a*) $\sigma = 1$, (*b*) $\sigma = 0.01$. In each case the lower half of the figure shows the flow in the lower boundary layer while the upper half shows the flow in the upper boundary layer.

layer and were calculated for $T = 0.63733$ and $P_{ext} = -1.0$ at the points indicated in figure 13. As the cross-stream pressure gradient is increased, the sharp corners in the core streamline displacement at the beginning and end of the membrane section are smoothed. The disturbance to the upper boundary layer is noticeably less, with both a much smaller and smoother disturbance to the streamlines and a reduction in the amount of dissipation there. The region of increased dissipation extends further downstream for smaller σ. The general shape of the region of dissipation agrees with

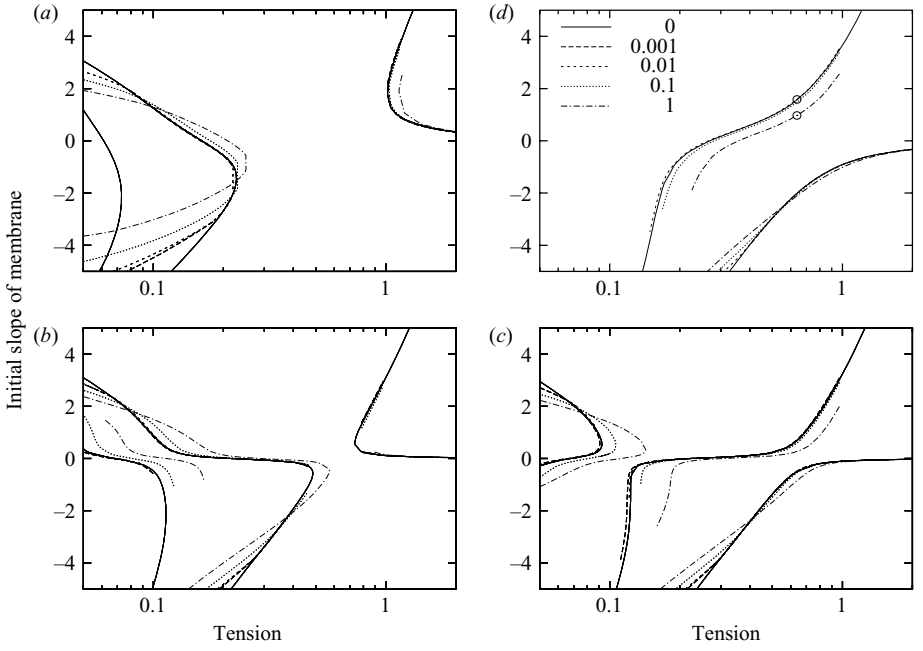

FIGURE 13. Partial bifurcation diagrams plotted for $\sigma = 0, 0.001, 0.01, 0.1, 1$ and (*a*), $P_{ext} = 1$, (*b*) $P_{ext} = 0.1$, (*c*) $P_{ext} = -0.1$, (*d*) $P_{ext} = -1$. The two marked points in (*d*) at $T = 0.63733$ indicate the points corresponding to the plots in figure 12.

that shown by Luo & Pedley (1998) although their work concerns unsteady flow past a deformation of size comparable with the channel width. In particular, the correlation of dissipation with vorticity leads to regions of high dissipation on the walls in the constricted region and tongues extending downstream.

Figure 13 shows the variation in the bifurcation diagram in $(F_x(0), T)$-space plotted for $P_{ext} = 1, 0.1, -0.1$ and 1 as σ is increased from zero. When σ is non-zero only the branches at higher values of the tension have been plotted since these are sufficient to illustrate the behaviour.

Increasing the value of σ has little qualitative effect on the form of the bifurcation diagrams in the parameter range examined. In general the various branches are collapsed towards the horizontal axis and move to slightly higher values of the tension.

We note, however, that the pressure in this calculation is fixed at the upstream end of the flow domain rather than at the start of the membrane section. In the studies with negligible cross-stream pressure gradient the pressure was fixed at the upstream end of the membrane section because in this case there is no pressure drop prior to reaching the start of the membrane. Consequently, the position at which the pressure is considered to be fixed when comparing the results is some distance upstream of the membrane.

If the wall deformation (a constriction, say) were specified and σ reduced while holding the transmural pressure far upstream constant, this would lead to a reduction in the internal pressure at the upstream end of the deformation since the flow experiences a greater degree of adjustment upstream of the obstacle. A more positive transmural pressure, i.e. larger P_{ext}, would then lead to a greater curvature of the

membrane inwards and hence suggests that a smaller value of the initial slope will be required for a solution.

4.4. *Downstream transmural pressure*

The transmural pressure at the downstream end of the membrane for the data set described in § 4.2 is plotted in figure 14. The sign of the downstream transmural pressure depends upon whether the membrane is collapsed or dilated at the downstream end; as previously observed, the sign is fixed over any given solution branch. Thus, the downstream transmural pressure is bounded away from zero for all solutions except the trivial one, and there are no eigenmode solutions at zero downstream transmural pressure as there are when $P_{ext} = 0$. Solutions that include regions of reversed flow are indicated by dashed lines, as in figure 6.

It is noticeable that the branches at negative downstream transmural pressure, i.e. those dilated at the downstream end, appear to have a minimum attainable value of the downstream transmural pressure for any given value of P_{ext}. The branches terminate when the membrane deformation and degree of flow reversal become excessive and the solution fails to converge. This suggests that lower (more negative) values of the downstream transmural pressure will arise only for membrane shapes whose distortion is too great for this method to converge.

Consideration of these results indicates that the behaviour of the system when the downstream transmural pressure is held fixed will be significantly different from that described in § 4.2 for fixed upstream transmural pressure. Graphs of the predicted behaviour are shown in figure 15. These show the form of the solution branches in the $(T, F_x(0))$-plane, for given values of the downstream transmural pressure. The available data points are shown, and the curves joining them are extrapolated from knowledge of the general behaviour of the system. While we have reasonable confidence in the curves for small absolute values of the downstream transmural pressure, the larger negative values in particular are not expected to be accurate, in particular the large loops on the $P_{ext} - P(1) = -2$ curve. Moreover, as indicated above, large negative values of the downstream transmural pressure will be associated with deformations larger than this method can handle.

In contrast with the behaviour seen when the upstream transmural pressure is fixed, the available data appear to indicate that solutions exist at all values of the tension for each value of the downstream transmural pressure. As the solution branch is followed from high to low tension, the mode of the solution increases; each time the upstream gradient passes through zero, a further extremum is added into the membrane shape. Furthermore, for P_{ext} sufficiently negative there appear to be ranges of the tension for which the solution is non-unique.

5. Discussion

5.1. *Summary of findings*

Application of a combination of analytic and numerical techniques to a high-Reynolds-number long-wavelength asymptotic analysis of the steady flow in a two-dimensional collapsible channel has revealed the rich structure of this part of the solution space. This has been examined in most detail at zero cross-stream pressure-gradient σ, when the solutions in the upper and lower boundary layers are identical.

The bifurcation structure is considered first for fixed upstream transmural pressure, P_{ext}, and variable tension. When P_{ext} is zero, the trivial solution undergoes an apparently infinite sequence of transcritical bifurcations as the tension is reduced

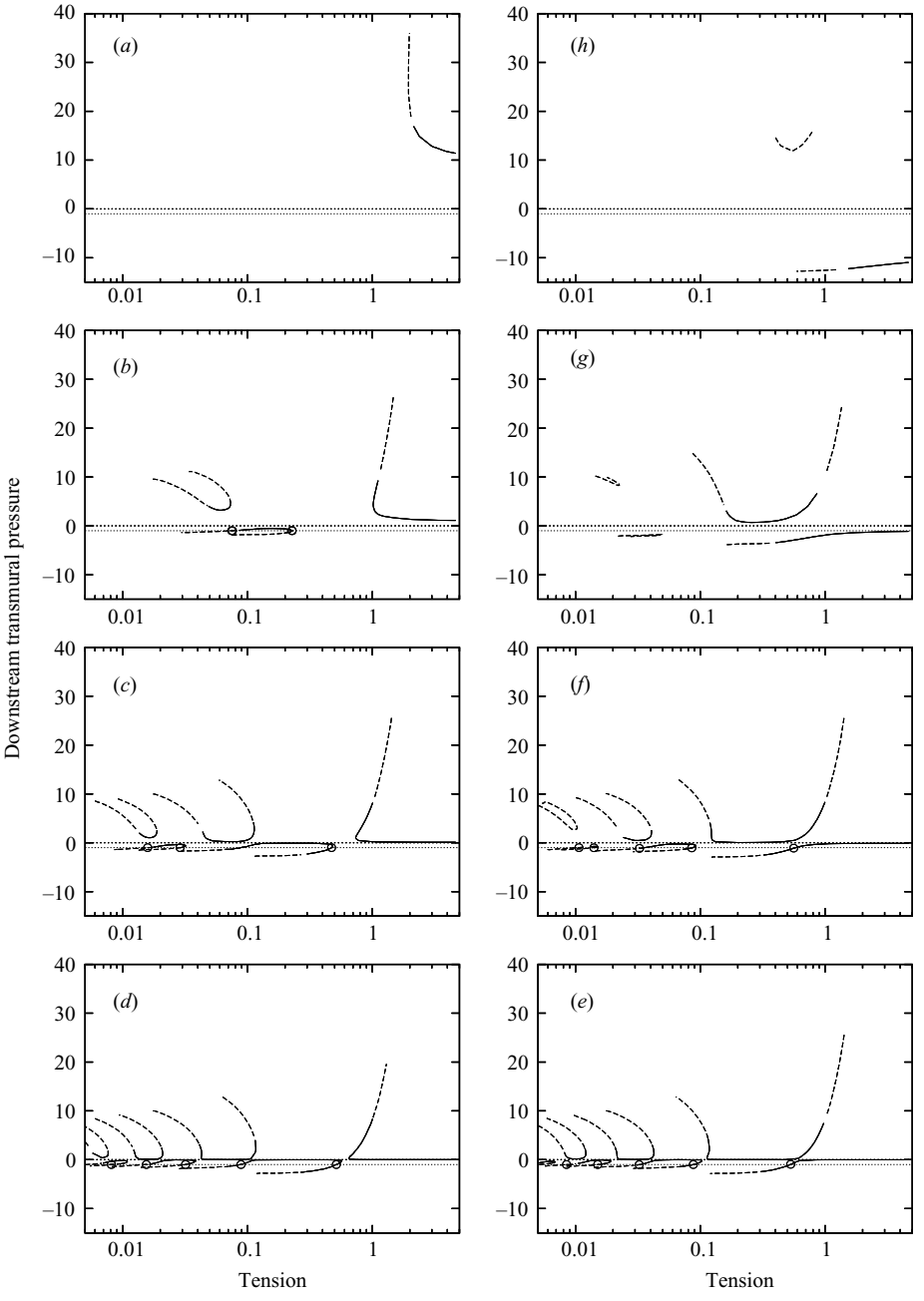

FIGURE 14. Downstream transmural pressure produced by each of the solutions shown in figure 6. Results are plotted for P_{ext} = (*a*) 10, (*b*) 1, (*c*) 0.1, (*d*) 0.01, (*e*) −0.01, (*f*) −0.1, (*g*) −1 and (*h*) −10; the solid and dashed lines indicate flows with and without regions of flow reversal. Solutions for which $P_{ext} - P(1) = -1$ (dotted line) are marked; these are used to construct the $P_{ext} - P(1) = -1$ curve in figure 15.

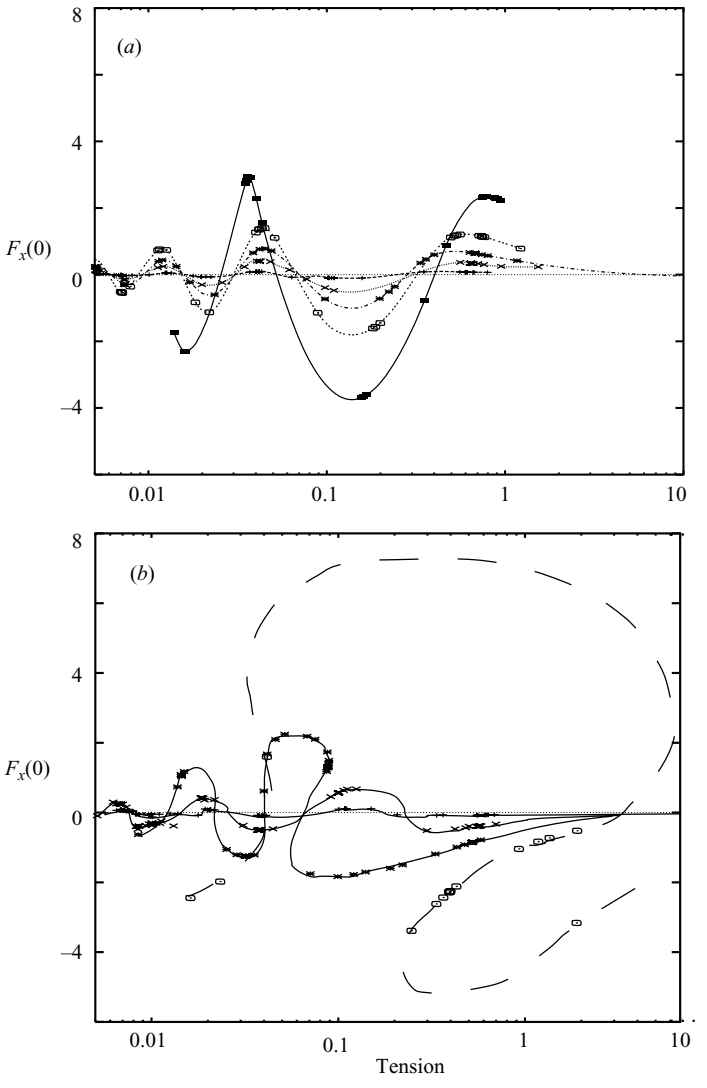

FIGURE 15. Graphs showing tension on the horizontal axis and the upstream slope of the membrane on the vertical axis. Points and curves plotted for (*a*) $P_{ext} - P(1) = 0, 0.1, 0.5, 1, 2, 5$ and (*b*) $P_{ext} - P(1) = 0, -0.1, -0.5, -1, -2$. The larger values of $|P_{ext} - P(1)|$ correspond to curves with greater oscillations of $|F_x(0)|$; the curve representing $P_{ext} - P(1) = 0$ is the axis $F_x(0) = 0$. The curves give only a rough indication of the behaviour between the known data points; in particular that drawn for $P_{ext} - P(1) = -2$ (long-dashed curve) is highly speculative.

towards zero. At non-zero upstream transmural pressure, the symmetry is broken and as its magnitude increases the low-tension branches are sequentially eliminated in a series of bifurcations until only one (two) branches remain for positive (negative) P_{ext}. This gives rise to ranges of the tension for which no steady solution exists under the imposed restrictions.

The behaviour of the system on fixing the downstream transmural pressure and varying the tension is very different. The (incomplete) results suggest that solutions exist for all values of the tension and downstream transmural pressure difference,

becoming non-unique for downstream transmural pressures below some (negative) threshold; we recall that negative transmural pressure corresponds to a membrane that is distended at the downstream end. Very negative downstream transmural pressure is associated with membrane deformations greater than can be handled with this method, although a qualitative indication of the expected behaviour may be extrapolated from the results for smaller deformations.

When the cross-stream pressure gradient is non-zero, the first few branches in the bifurcation diagrams appear qualitatively similar. Linearized analysis, however, shows that the number of transcritical bifurcations from the trivial solution occurring at zero upstream transmural pressure reduces with increasing σ, the last pair vanishing at $\sigma \approx 2.2$. This suggests that progressively fewer branches will be present at higher values of σ; the nonlinear results presented here at non-zero σ cover only branches that remain in existence for the range of σ considered.

We have also demonstrated that, in general, the leading-order contribution to the dissipation in the system has contributions both from the original Poiseuille flow and from the boundary layers. The dissipation arising from perturbations in the core is a higher-order term. Further, the greatest boundary-layer dissipation typically occurs over inward-sloping-wall regions, where the flow is being constricted. This contrasts with the assumption used in some previous models, e.g. that of Cancelli & Pedley (1985), that a turbulent jet is produced downstream of the constriction, the bulk of the dissipation occurring in this region.

5.2. *Comparison with Navier–Stokes computations*

The previous work most closely related to this paper is that of Luo & Pedley (2000) (referred to henceforth as LP), because there too the upstream transmural pressure difference was prescribed while the (steady) flow rate through the system was varied. There are, of course, many differences: in LP the membrane length was only five times the channel width, the Reynolds-number range was limited (up to 1000) and the membrane displacement was large. Nevertheless, multiple steady states were found in some parameter ranges and it is worth examining in more detail whether they may be related to those found here.

The type of non-uniqueness found by LP is most easily seen in plots such as those in figure 16, in which the Reynolds number Re is plotted against the pressure difference P^L_{ud} between the upstream and downstream ends of the channel, the different curves being for different values of the upstream transmural pressure difference, P^L_{ue} (the superfix L refers to the non-dimensionalization in LP). When that quantity is large enough, the computation reveals three possible steady flows for a finite, or in some cases possibly infinite, range of values of P^L_{ud}. The membrane tension is the same for all the curves. The three branches of solution correspond to different membrane shapes: on the uppermost branch, the membrane is everywhere displaced outwards; on the lowest branch it is indented either everywhere or over most of its length; and on the middle branch it is also always indented at the downstream end, and sometimes everywhere (see figure 17 for an example).

To compare parameter values between this work and that of LP, we need to take note of the different non-dimensionalizations of membrane tension and of external pressure, and also of the effects of the inclusion of rigid segments up- and downstream of the membrane section (with lengths of 5 and 30 channel widths respectively). In the present paper the dimensional tension $\hat{T}$ is given by

$$\hat{T} = \rho \bar{U}^2 a \lambda^2 \epsilon T = \rho \bar{U}^2 a (\lambda^7/Re)^{1/3} T, \tag{5.1a}$$

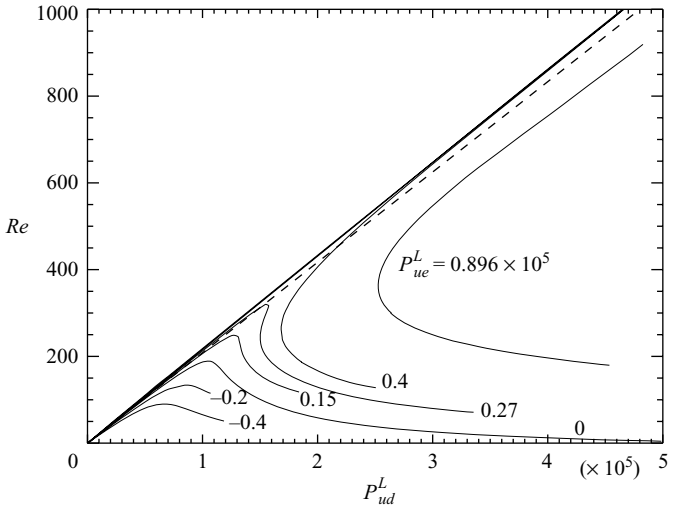

FIGURE 16. Steady solutions obtained by LP for $\beta = 35$ and $P^L_{ue}/10^5 = -0.4, -0.2, 0, 0.15, 0.27, 0.4$ and 0.896. The dashed line indicates the results obtained for Poiseuille flow in the undeformed channel. (Reproduction of LP figure 5.)

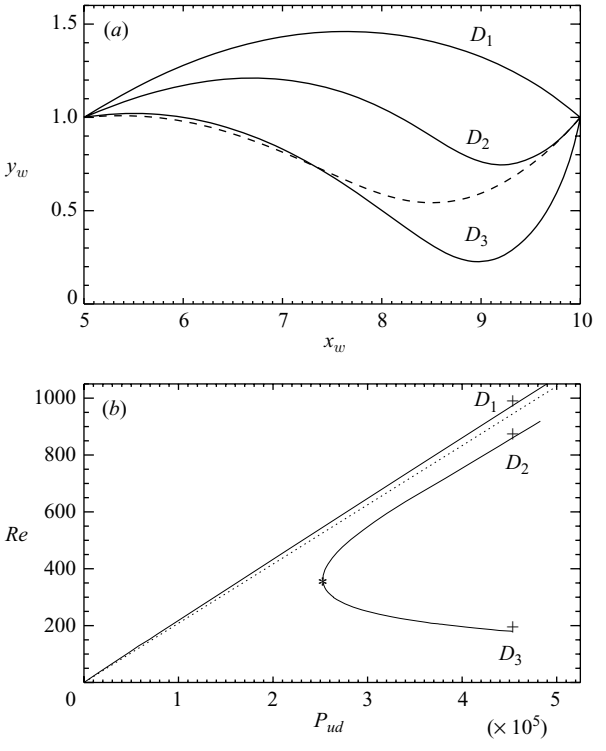

FIGURE 17. (*a*) Membrane shapes and (*b*) (*Re*, P_{ud})-curve; $\beta = 35$, $P_{ue} = 0.896 \times 10^5$. The thin dashed line in (*a*) is the wall shape at the turning point $*$ in (*b*). Points D_1, D_2, D_3 are examples of multiple solutions at the same driving pressure. The dotted line in (*b*) represents Poiseuille flow in an undeformed channel. (Reproduction of LP figure 9*a*.)

from (2.5), the line below (2.17) and (2.8). LP, however, took

$$\hat{T} = \rho \bar{U}^2 a \tilde{T}_0 / Re^2 \beta, \tag{5.1b}$$

where $\tilde{T}_0 \approx 1.61 \times 10^7$ and β was the parameter that varied as $\hat{T}$ was varied. Note that the Reynolds-number dependence means that fixing β is equivalent to fixing $\hat{T}$, independent of the flow rate. Combining (5.1*a*) and (5.1*b*) we obtain

$$T = \lambda^{-7/3} Re^{-5/3} \tilde{T}_0 / \beta.$$

The non-dimensionalizations of pressure, in this work and LP respectively, are

$$\hat{p} = \rho \bar{U}^2 \epsilon^2 P \quad \text{and} \quad \hat{p} = \rho \bar{U}^2 P^L / Re^2, \tag{5.2}$$

whence, using (2.8),

$$P = \lambda^{-2/3} Re^{-4/3} P^L.$$

The quantity held constant on the curves of figure 16 is

$$P^L_{ue} = P^L_u - P^L_e,$$

where P^L_e is the (scaled) external pressure and P^L_u is the (scaled) pressure at the channel entrance, which is five channel widths upstream of the start of the membrane and was taken to be zero. For comparison with the current study, we require

$$P^L_{ext} = P^L_e - P^L_0,$$

where P^L_0 is the internal pressure at the upstream end of the membrane. The viscous pressure drop in the rigid segment is approximately that given by Poiseuille flow (a Poiseuille profile is assumed at the entrance). Thus

$$P^L_{ext} \approx 60Re - P^L_{ue}.$$

We cannot expect to get a good comparison of the driving pressure difference, since the pressure drop in the downstream rigid section is unknown. If, however, we use a Poiseuille pressure drop as a crude approximation, we may approximate the pressure drop along the membrane section, P_{01}, by

$$P^L_{01} \approx P^L_{ud} - 420Re.$$

In the present analysis, moreover, the Poiseuille pressure gradient is formally a higher-order term and is neglected. We may therefore consider the Poiseuille pressure drop over the length of the membrane, $P^L = 60Re$, to give an indication of the expected inaccuracy of any comparison.

Hence, if we consider the curves $P^L_{ue} = 0.896 \times 10^5$ in figure 16 and choose $Re = 500$, $\lambda = 5$ we see that there are two solutions, for which

$$P_{ext} \approx -5.14, \quad \epsilon \approx 0.215,$$

and P^L_{ud} is approximately equal to 2.3×10^5 or 2.8×10^5, i.e.

$$P(x = 1) \approx 1.7 \text{ or } 6.0.$$

We expect a disagreement of the order of $P^L = 60Re$ ($P = 2.6$) between these figures and those from the current boundary-layer analysis. Moreover, $\beta = 35$ corresponds to

$$T \approx 0.342,$$

which is quite a small value. Thus the two possible flows for $Re = 500$ should be found on a bifurcation diagram between our figures 6(*g*) and 6(*h*). Such a diagram is

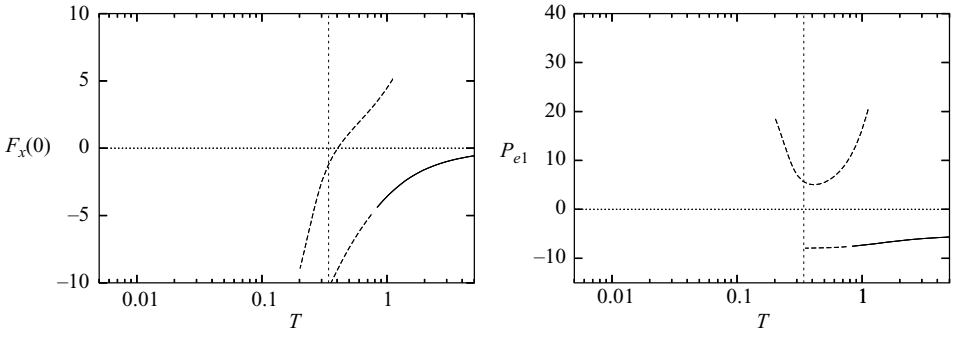

FIGURE 18. Upstream slope and downstream transmural pressure, $P_{e1} = P_{ext} - P(1)$, for $P_{ext} = -5.14$. The solid and dashed lines indicate flows with and without regions of flow reversal. The vertical line $T = 0.342$ for comparison with LP has also been drawn.

plotted in figure 18; the lower solution branch does not extend quite to $T = 0.342$ but the reason is that the membrane has become too deformed for our analysis. We may therefore conclude that there are indeed two solutions indicated at $T = 0.342$, with $P(1) \approx 2.8$ or -10.7. Since $|P_{ext}|/T$ is around 15, rather than $O(1)$ as required for our nonlinear analysis let alone $\ll 1$ as required for the linearized analysis (see (2.17) and (2.22)), the agreement with the values obtained via the crude approximation from LP is not particularly good, but the disagreement is of the order predicted.

For higher Re, P_{ext} and T are both smaller for the same values of β and P_{ue}^L; for lower Re, they are larger. As T is reduced (i.e. β or Re increased), solutions on the rightmost branch in figure 6(a–c) cease to exist at a critical value of T. This is equivalent to the non-existence of solutions in figure 16 for $P_{ue}^L \leqslant 0.27$ as Re is increased above a given value. In particular we note that positive values of P_{ext} arise only for (a) negative values of P_{ue}^L at small Reynolds number ($Re < 200$) and (b) large P_{ue}^L and Reynolds number.

We may conclude with some confidence that the steady solutions computed by LP from the full Navier–Stokes equations are equivalent to solutions on those branches of our diagrams, derived from the boundary-layer equations, that persist at large external pressure.

5.3. *Stability*

The stability of the solutions found in this paper has not yet been considered. It might be expected that the high-tension branch would be the most likely to be stable, and many of the other branches unstable, but this requires investigation. We note that LP did compute the stability of their solutions and found that whether a flow was stable could depend on whether the upstream pressure or the upstream flow rate was held constant, the latter being more likely to lead to stability on the lowest solution branch (figure 16). In general solutions on the upper or leftmost branch, on which the flow rate increases with P_{ud}^L for all P_{ue}^L, are stable.

We also recall that Jensen & Heil (2003) found stability whenever the inflow rate was held fixed and instability for fixed upstream pressure only if the length of the rigid part of the channel downstream, L_2, was greater than that upstream, L_1. For comparison purposes, we note that the critical Reynolds number for instability, when $L_2 > L_1$, was given by Jensen & Heil (2003) as

$$Re_c \approx r_{c0}^2 (T^J)^{1/2},$$

Reynolds number	Re	$=$	$\bar{U}a/\nu$	$\propto \bar{U}$
boundary layer thickness	ϵ	$=$	$(\lambda/Re)^{1/3}$	$\propto \bar{U}^{-1/3}$
cross-stream pressure gradient	σ	$=$	$6/5\lambda^2\epsilon$	$\propto \bar{U}^{1/3}$
pressure	P	$=$	$\epsilon^{-2}\rho^{-1}\bar{U}^{-2}\hat{p}$	$\propto \bar{U}^{-4/3}\hat{p}$
tension	T	$=$	$\epsilon^{-1}\rho^{-1}\bar{U}^{-2}\lambda^{-2}a^{-1}\hat{T}$	$\propto \bar{U}^{-5/3}\hat{T}$
velocity	U	$=$	$\epsilon^{-1}\bar{U}^{-1}\hat{u}$	$\propto \bar{U}^{-2/3}\hat{u}$
location of membrane	F	$=$	$\hat{F}/a\epsilon$	$\propto \bar{U}^{1/3}\ \hat{F}$

TABLE 1. Relation of boundary-layer parameters and variables to dimensional quantities.

where T^J is their dimensionless tension ($= \hat{T}/\rho\bar{U}^2a$ in the notation of this paper), and r_{c0} is a constant that depends on L_1 and L_2 and is supposedly $O(1)$ as $T^J \to \infty$. In our notation this gives

$$Re_c \approx r_{c0}^2 T^{1/2}\lambda\,(\lambda/Re_c)^{1/6}\,,$$

i.e.

$$Re_c \approx r_{c0}^{12/7} T^{3/7}\lambda.$$

Alternatively, for a given Re, the critical tension below which the flow is unstable is given by

$$T_c = r_{c0}^{-4}\,(Re/\lambda)^{7/3}\,. \tag{5.3}$$

For $Re = 500$ and $\lambda = 5$ and r_{c0} in the range 3 to 10, as suggested by the results of Jensen & Heil, this gives T_c in the range 4.6×10^4 down to 570. The asymptotic theory of Jensen & Heil is valid only if $T^J \gg Re$, and these numbers confirm that their theory applies at much larger values of T than those considered here.

5.4. *Implications for experiment*

It would be desirable to compare the results of this paper, those of LP and those of Jensen & Heil (2003) with a suitable experiment. However, it has proved very difficult to set up a two-dimensional or annular experiment, even approximately (Ikeda *et al.* 1998); experiments are easy to set up only in tubes, not channels. Nevertheless, it is worth considering what parameter values it might be possible to achieve in principle. The difficulty, as we shall see, would be in finding a material for the membrane that can be stretched flat with a sufficiently low value of tension, at least when the working fluid is water.

For a fixed channel geometry and working fluid, the quantities λ, a, ρ and ν are constants and cannot be changed during an experiment. However, the external and upstream (or downstream) pressure, the membrane tension and the Reynolds number can all be varied. The relevant dimensionless parameters and variables are listed in table 1, from which the relations between them can be seen. In particular, we note that our scalings mean that all variables vary with the inlet flow velocity $\bar{U}$, so our study can be best thought of as corresponding to a fixed flow velocity (or Re) and variable $\hat{P}_{ext}$ and $\hat{T}$. We should also recall that the validity of the boundary-layer theory requires that Re and λ satisfy $1 \ll \lambda \ll Re \leqslant \lambda^7$.

In the attempted experiments of Ikeda *et al.* (1998), water was the working fluid ($\rho = 10^3\,\mathrm{kg\,m^{-3}}$, $\nu \approx 10^{-6}\ \mathrm{m^2\,s^{-1}}$), the channel width a was 5 mm, λ took the value 5, and Reynolds numbers of several hundred were employed. Taking $Re = 500$, this

gives $\bar{U} = 0.1$ m s^{-1}. The corresponding values of $\hat{T}$ and $\hat{p}_{ext}$, from (5.1*a*) and (5.2), are

$$\hat{T} = 0.27T \text{ N m}^{-1}, \quad \hat{p}_{ext} = 0.46P_{ext} \text{ Pa}.$$

Noting that the surface tension of water in air is about 7 N m^{-1}, and the tension in a thin latex membrane of Young's modulus 5×10^5 Pa, thickness 0.5 mm and stretch ratio 1.1 is about 25 N m^{-1}, it is clear that the value of T corresponding to a feasible experiment would have to be considerably larger than the values that have proved to be most interesting here. Similarly, since 1 cm H_20 corresponds to 100 Pa, $|P_{ext}|$ would normally be very large too, if it were not zero. The only way to make the tension and pressures feasible is to increase $\bar{U}$ significantly, and if the Reynolds number is not to be changed this requires the use of a much more viscous fluid.

The authors would like to thank the Engineering and Physical Sciences Research Council for their support while this work was performed in the late 1990s: J. C. G. for a Research Studentship and T. J. P. for a Senior Fellowship.

REFERENCES

Bertram, C. D., Raymond, C. J. & Pedley, T. J. 1991 Application of non-linear dynamics concepts to the analysis of self-excited oscillations of a collapsible tube conveying flow. *J. Fluids Struct.* **5**, 391–426.

Cai, Z. X. & Luo, X. Y. 2003 A fluid-beam model for flow in a collapsible channel. *J. Fluids Struct.* **17**, 125–146.

Cancelli, C. & Pedley, T. J. 1985 A separated flow model for collapsible tube oscillations. *J. Fluid Mech.* **157**, 375–404.

Conrad, W. A. 1969 Pressure-flow relationships in collapsible tubes. *IEEE Trans. Bio-Med. Engng* **16**, 284–295.

Gajjar, J. S. B. & Türkyilmazoğlu, M. 2000 On the absolute instability of the triple-deck flow over humps and near wedged trailing edges. *Phil. Trans. R. Soc. Lond.* A **358**, 3113–3128.

Grotberg, J. B. & Jensen, O. E. 2004 Biofluid mechanics in flexible tubes. *Annu. Rev. Fluid Mech.* **36**, 121–127.

Hazel, A. L. & Heil, M. 2003 Steady finite-Reynolds-number flows in three-dimensional collapsible tubes. *J. Fluid Mech.* **486**, 79–103.

Heil, M. & Jensen, O. E. 2003 Flows in deformable tubes and channels; theoretical models and biological applications. In *Flow in Collapsible Tubes and Past other highly Compliant Boundaries* (ed. P. W. Carpenter & T. J. Pedley), chap. 2. Kluwer.

Ikeda, T., Heil, M., Beaugendre, H. & Pedley, T. J. 1998 Experiments on flow in a two-dimensional collapsible channel. In *Abstracts of the Third World Congress of Biomechanics, Sapporo, Japan* (ed. Y. Matsuzaki, T. Nakamura & E. Tanaka), p. 38.

Jensen, O. E. 1990 Instabilities of flow in a collapsed tube. *J. Fluid Mech.* **220**, 623–659.

Jensen, O. E. & Heil, M. 2003 High-frequency self-excited oscillations in a collapsible-channel flow. *J. Fluid Mech.* **481**, 235–268.

Jensen, O. E. & Pedley, T. J. 1989 The existence of steady flow in a collapsed tube. *J. Fluid Mech.* **206**, 339–374.

Kamm, R. D. & Shapiro, A. H. 1979 Unsteady flow in a collapsible tube subjected to external pressure or body forces. *J. Fluid Mech.* **95**, 1–78.

Katz, A. I., Chen, Y. & Moreno, A. H. 1969 Flow through a collapsible tube. *Biophys. J.* **9**, 1261–1279.

Keller, H. B. 1971 A new difference scheme for parabolic problems. In *Numerical Solution of Partial Differential Equations -I* (ed. B. Hubbard), pp. 327–350. Academic.

Keller, H. B. 1978 Numerical methods in boundary layer theory. *Annu. Rev. Fluid Mech.* **10**, 417–433.

Luo, X. Y. & Pedley, T. J. 1995 A numerical simulation of steady flow in a 2-D collapsible channel. *J. Fluids Struct.* **9**, 149–174.

Luo, X. Y. & Pedley, T. J. 1996 A numerical simulation of unsteady flows in a two-dimensional collapsible channel. *J. Fluid Mech.* **314**, 191–225.

Luo, X. Y. & Pedley, T. J. 1998 The effects of wall inertia on flow in a two-dimensional collapsible channel. *J. Fluid Mech.* **363**, 253–280.

Luo, X. Y. & Pedley, T. J. 2000 Multiple solutions and flow limitation in collapsible channel flows. *J. Fluid Mech.* **420**, 301–324.

Pedley, T. J. 1992 Longitudinal tension variation in collapsible channels. A new mechanism for the breakdown of steady flow. *Trans. ASME: J. Biomech. Engng* **114**, 60–67.

Pedley, T. J. 2000 Blood flow in arteries and veins. In *Perspectives in Fluid Dynamics* (ed. G. K. Batchelor, H. K. Moffatt & M. G. Worster), pp. 105–158. Cambridge University Press.

Pedley, T. J. & Luo, X. Y. 1998 Modelling flow and oscillations in collapsible tubes. *Theor. Comput. Fluid Dyn.* **10**, 277–294.

Reyhmer, T. A. & Flügge-Lotz, I. 1968 The interaction of a shock wave with a laminar boundary layer. *Intl J. Non-linear Mech.* **3**, 173–199.

Rothmayer, A. P. 1989 The viscous flow through symmetric collapsible tubes. *Mathematika* **36**, 153–181.

Shapiro, A. H. 1977 Steady flow in collapsible tubes. *Trans ASME: J. Biomech. Engng* **99**, 126–147.

Smith, F. T. 1976*a* Flow through constricted or dilated pipes and channels: Pt I. *Q. J. Mech. Appl. Maths* **29**, 343–364.

Smith, F. T. 1976*b* Flow through constricted or dilated pipes and channels: Pt II. *Q. J. Mech. Appl. Maths* **29**, 365–376.

Smith, F. T. 1977 Upstream interaction in channel flows. *J. Fluid Mech.* **79**, 631–655.

Smith, F. T. & Duck, P. W. 1980 On the severe non-symmetric constriction, curving or cornering of channel flow. *J. Fluid Mech.* **98**, 727–753.

Tutty, O. R. 1984 High Reynolds number viscous flow in collapsible tubes. *J. Fluid Mech.* **146**, 451–469.